

A KECK SPECTROSCOPIC SURVEY OF MS 1054-03 ($Z = 0.83$): FORMING THE RED SEQUENCE^{1,2}

KIM-VY H. TRAN^{3,4,5,6}, MARIJN FRANX⁶, GARTH D. ILLINGWORTH⁷,
PIETER VAN DOKKUM⁸, DANIEL D. KELSON⁹, JOHN P. BLAKESLEE¹⁰, AND MARC POSTMAN¹¹
Draft version September 16, 2018

ABSTRACT

Using a magnitude-limited, spectroscopic survey of the X-ray luminous galaxy cluster MS 1054-03, we isolate 153 cluster galaxies and measure MS1054's redshift and velocity dispersion to be $z = 0.8307 \pm 0.0004$ and $\sigma_z = 1156 \pm 82 \text{ km s}^{-1}$. The absorption-line, post-starburst ("E+A"), and emission-line galaxies respectively make up $63 \pm 7\%$, $15 \pm 4\%$, and $23 \pm 4\%$ of the cluster population. With photometry from HST/ACS, we find that the absorption-line members define an exceptionally tight red sequence over a span of ~ 3.5 magnitudes in i_{775} : their intrinsic scatter in $(V_{606} - i_{775})$ color is only 0.048 ± 0.008 , corresponding to a $(U - B)_z$ scatter of 0.041. Their color scatter is comparable to that of the ellipticals ($\sigma_{V_i} = 0.055 \pm 0.008$), but measurably smaller than that of the combined E+S0 sample ($\sigma_{V_i} = 0.072 \pm 0.010$). The color scatter of MS1054's absorption-line population is approximately twice that of the ellipticals in Coma; this difference is consistent with passive evolution where most of the absorption-line members ($> 75\%$) formed by $z \sim 2$, and all of them by $z \sim 1.2$. For red members, we find a trend ($> 95\%$ confidence) of weakening H δ absorption with redder colors that we conclude is due to age: in MS1054, the color scatter on the red sequence is driven by differences in mean stellar age of up to ~ 1.5 Gyr. We also generate composite spectra and estimate that the average S0 in MS1054 is $\sim 0.5 - 1$ Gyr younger than the average elliptical; this difference in mean stellar age is mainly due to a number of S0s that are blue (18%) and/or are post-starburst systems (21%).

Subject headings: galaxies: clusters: individual (MS 1054-03) – galaxies: elliptical and lenticular, cD – galaxies: fundamental parameters – galaxies: evolution

1. INTRODUCTION

Understanding how galaxies form and evolve in clusters continues to be a fundamental question in astronomy. The ages and assembly histories of galaxies in rich clusters test both stellar population models and hierarchical formation scenarios. Studies of the passive, red galaxies that dominate local clusters show that the bulk of their stars formed at $z > 2$ (Bower et al. 1992; Jørgensen et al. 1999; Trager et al. 2000) and indicate that the cluster population has not evolved strongly in the last ~ 8 Gyr. However, the current paradigm of hierarchical assembly (Peebles 1970) predicts that clusters continue to grow by accreting galaxies. Indeed, observations of clusters at $z > 0.3$ have revealed an increasing fraction of blue, star-forming galaxies at higher redshift (Butcher & Oemler 1984; Couch & Sharples 1987; Ellingson et al. 2001).

How to link the evolving cluster populations observed at intermediate redshifts ($0.3 < z < 1$) to the predominantly quiescent ones at $z \sim 0$ is a matter of much debate. Using

imaging from the *Hubble Space Telescope*, several studies find a deficit of S0 galaxies in $z \gtrsim 0.4$ clusters and argue that the observed excess of blue galaxies must evolve into the missing S0s (Dressler et al. 1997; Lubin et al. 2002; Tran et al. 2005a; Postman et al. 2005). However, this implies that S0s are younger than the ellipticals, and such a difference in mean age is at odds with other HST studies of $z \sim 0.3 - 0.5$ clusters that find the S0s to be as old as the ellipticals (Ellis et al. 1997; Kelson et al. 2000). It may be that the fractional age difference between Es and S0s is negligible at $z \lesssim 0.4$, but that such an imprint is still visible at $z \gtrsim 0.8$ when even massive cluster galaxies are at most only ~ 4 Gyr old (Thomas et al. 2005).

This debate raises the more general issue of how the color-magnitude relation, and subsequently the red sequence, forms and evolves. The ellipticals and S0 galaxies in local clusters define a narrow ridge on the color-magnitude diagram that indicates homogeneously old ages (Sandage & Visvanathan 1978; Bower et al. 1992; Kodama et al. 1998), and the low color scatter in

¹ Based on observations obtained at the W. M. Keck Observatory, which is operated jointly by Caltech and the University of California.

² Based on observations with the NASA/ESA Hubble Space Telescope, obtained at the Space Telescope Science Institute, which is operated by the Association of Universities for Research in Astronomy, Inc., under NASA contract NAS 5-26555.

³ NSF Astronomy & Astrophysics Fellow

⁴ NOVA Fellow

⁵ Harvard-Smithsonian Center for Astrophysics, 60 Garden Street, Cambridge, MA 02138

⁶ Leiden Observatory, Leiden University, Niels Bohrweg 2, 2333 CA Leiden, The Netherlands

⁷ University of California Observatories/Lick Observatory, University of California, Santa Cruz, CA 95064

⁸ Department of Astronomy, Yale University, New Haven, CT 06520-8101

⁹ Observatories of the Carnegie Institution of Washington, 813 Santa Barbara Street, Pasadena, CA, 91101

¹⁰ Department of Physics and Astronomy, Washington State University, Pullman, WA 99164-2814

¹¹ Space Telescope Science Institute, 3700 San Martin Drive, Baltimore, MD 21218

the E+S0 members has been confirmed to $z \sim 0.9$ (Stanford et al. 1998). However, if the galaxy types differ in mean stellar age (*e.g.* Poggianti et al. 2001), this implies that the red sequence continued to assemble after it was initially seeded at higher redshift ($z > 2$). For example, faint ($L < L^*$) S0s are inferred to evolve from fading blue galaxies at $z \lesssim 0.8$, thus they appear on the red sequence at lower redshifts compared to the more massive S0s (Tran et al. 2005a; Holden et al. 2006), and the resulting red sequence galaxies would have heterogeneous star formation histories (van Dokkum et al. 1998; Bower et al. 1998). Therefore determining how the red sequence assembles by measuring, *e.g.* how the color scatter evolves, provides useful tests of cluster formation models (Kauffmann 1995; Baugh et al. 1996; Diaferio et al. 2001).

The main challenges for studying cluster populations at intermediate redshifts and how they evolve are 1) isolating the members and 2) obtaining the high resolution imaging needed to determine morphologies. Although photometric surveys have an advantage in terms of surveyed area, they have inherent and possibly large uncertainties due to field corrections. Only with spectroscopy can we confidently isolate cluster galaxies from the field. Spectroscopy also provides useful and independent diagnostics for separating members into absorption-line, emission-line, and post-starburst (“E+A”; Dressler & Gunn 1983) galaxies, and for determining mean stellar ages to identify, *e.g.* the oldest cluster galaxies.

Motivated by these issues, we present an extensive magnitude-limited spectroscopic survey of MS 1054–03, a massive, X-ray luminous galaxy cluster first detected in the *Einstein* Medium Sensitivity Survey (Gioia & Luppino 1994) and spectroscopically confirmed to be at $z = 0.83$ by Donahue et al. (1998). With medium resolution spectroscopy from Keck/LRIS (Oke et al. 1995), we isolate 153 cluster galaxies and measure their spectral indices. We pair the spectroscopy with imaging from the *Advanced Camera for Surveys* (Ford et al. 1998) that provides accurate colors and magnitudes as well as morphological types. To improve our spectral signal-to-noise, we also generate composite spectra for the different spectral and morphological classes, and compare their spectral indices to stellar population models.

Our primary goal is to trace how the red sequence assembles. To do so, we first identify the oldest cluster galaxies and determine whether they define a tight color-magnitude relation over a wide range in luminosity. We then compare the colors and spectral diagnostics of the different galaxy classes to identify any trends with, *e.g.* age.

The paper is organized as follows: In §2, we describe the HST imaging and Keck spectroscopy, the completeness of our spectroscopic survey, and define the spectral types. We determine MS1054’s mean redshift, velocity dispersion, virial mass, and degree of substructure in §3. We analyse the color-magnitude diagram in §4 and the composite spectra in §5. We discuss how the red sequence forms in §6 and summarize our results in §7. Throughout the paper, we use $\Omega_M = 0.3$, $\Omega_\Lambda = 0.7$, and $H_0 = 70h$ km s $^{-1}$ Mpc $^{-1}$. At $z = 0.83$, this corresponds to a projected scale of $7.6h^{-1}$ kpc arcsec $^{-1}$. Note that we use a different value for H_0 than in our earlier papers on MS1054.

2. OBSERVATIONS

2.1. HST/WFPC2 Imaging

In May 1998, a $\sim 5' \times 6'$ mosaic of the MS 1054–03 field was taken with WFPC2 on the *Hubble Space Telescope*. Six slightly overlapping pointings were taken in both the F606W and F814W filters. A full explanation of the WFPC2 image reduction is described in van Dokkum et al. (2000, hereafter vD00).

Because our spectroscopic survey was designed primarily from the WFPC2 imaging, we use the WFPC2 photometry to determine our spectroscopic completeness (§2.4.2). We measure total magnitudes and galaxy colors using SEXTRACTOR (Bertin & Arnouts 1996) where galaxy colors were measured within a $1''$ diameter apertures; note this is different from vD00 where colors were measured within one effective radius. At $z = 0.83$, V_{606} and I_{814} approximately correspond to redshifted U and B . We stress that we only use the WFPC2 photometry in §2.3. For the remainder of the paper, we use the magnitudes and colors measured from the ACS imaging.

2.2. HST/ACS Imaging

For the most of our analysis, we use the photometry and morphological information derived from imaging taken with the HST *Advanced Camera for Surveys* (Ford et al. 1998). A 2×2 overlapping mosaic ($5.8' \times 5.8'$) was taken in F775W and F850LP in December 2002, and the same pattern executed in F606W in January/February 2004. A detailed description of the ACS image reduction is presented in Blakeslee et al. (2006, hereafter B06). To summarize, B06 fitted the 2-D surface brightness distribution of each galaxy using a Sérsic profile; they then measured AB magnitudes and colors within the effective radius. We use their AB magnitudes and galaxy colors in our analysis; we also adopt their nomenclature and refer to the AB magnitudes in F775W as i_{775} , and the galaxy color corresponding the difference between F606W and F775W as $(V - i_{775})$. The characteristic AB magnitude m^* for the cluster population is $i_{775} = 22.3$ (Goto et al. 2005).

All galaxies on the ACS mosaic brighter than $i_{775} = 23.5$ were visually classified by Postman et al. (2005, hereafter P05). Many of the same galaxies also were classified earlier by vD00 using the WFPC2 imaging ($I_{814} < 22$). The WFPC2 imaging revealed a large number of galaxy-galaxy mergers (van Dokkum et al. 1999) that have since been spectroscopically confirmed by Tran et al. (2005b). With the higher resolution ACS imaging, P05 were able to morphologically classify the galaxies making up these mergers, most of which are bulge-dominated systems. We direct the reader to P05 for a thorough discussion on the morphological classifications and comparisons between the two surveys. For our analysis, we use the Hubble types assigned by P05 but also note the merging systems identified by vD00. P05 assigned the following morphological types: elliptical ($-5 \leq T \leq -3$); S0 ($-2 \leq T \leq 0$); and spiral+irregular ($1 \leq T \leq 10$). The Hubble types as well as ACS photometry for the cluster galaxies are listed in Table 1.

2.3. Transforming to Rest-frame Johnson Filters

Throughout most of this paper, we use observed AB colors and magnitudes from ACS; as stated in B06, this enables us to preserve the model-independence of our results. However, we do use rest-frame colors and magnitudes for part of our analysis, and we follow B06 to transform between the observed ACS filters and redshifted Johnson filters. In B06, the ACS/WFC photometry is transformed by computing standard UBV rest-frame colors and observed ACS/WFC system colors for the same models redshifted to $z = 0.83$. From B06 and Jee et al. (2005), we transform observed V_{606} , i_{775} , and z_{850} to rest-frame Johnson colors and magnitudes using:

$$B_z = i_{775} - 0.16(i_{775} - z_{850})^2 - 0.22(i_{775} - z_{850}) + 0.73 \quad (1)$$

$$(U - B)_z = 0.85(V_{606} - i_{775}) - 1.01 \quad (2)$$

$$(U - V)_z = 0.95(V_{606} - z_{850}) - 0.91 \quad (3)$$

Thus to transform the color scatter in, *e.g.* observed $(V_{606} - i_{775})$ (hereafter we use V to refer to V_{606}) to Johnson $(U - B)_z$, we simply multiply by 0.85.

2.4. Keck/LRIS Spectroscopy

2.4.1. Observations & Reduction

Using the *Low Resolution Imaging Spectrogram* (LRIS; Oke et al. 1995) on Keck, we carried out a spectroscopic survey of the MS1054 field from February 1997 to June 2001; the spectra were collected during six observing runs. To select targets for the multi-slit masks, two object catalogs were used. The first catalog was created from a 900 second Keck I image ($1''$ seeing) centered on the Brightest Cluster Galaxy (BCG). Objects were detected with FOCAS Valdes (1982) and I magnitudes determined for a $3''$ diameter aperture. Spectra taken in February 1997 and February 1998 were selected from the Keck I catalog and are of objects with $I < 20.5$; the BCG has $I = 17.5$ mag. No morphological selection was applied.

After obtaining our wide-field HST/WFPC2 imaging in May 1998, a second object catalog was generated. Objects were detected and best magnitudes determined from the WFPC2 I_{814} mosaic using SExtractor Bertin & Arnouts (1996); the BCG has $I_{814} = 19.5$ mag. Spectroscopic targets for runs in January, February, and March 1999 as well as June 2001 were selected from the HST/WFPC2 object catalog. As in the earlier runs, target selection was based primarily on magnitude ($I_{814} \leq 23.5$) and not color; in only one mask was morphology used to select targets as we wished to obtain redshifts of close galaxy pairs.

A total of 20 multi-slit masks (field of view $\sim 7' \times 7'$) containing 711 targets were observed; many objects were observed in multiple masks. The multi-slit masks included both masks designed to measure redshifts ($t_{\text{exp}} \sim 2000$ sec) and masks to measure internal velocity dispersions ($t_{\text{exp}} \geq 10000$ sec) with redshift fillers; many of the targets were observed in multiple masks. The slits were $1''$ wide and, depending on the grating used, the spectral resolution (FWHM) ranged from 9–13 Å with higher spectral resolution (5–6 Å) used for the dispersion masks.

To reduce the spectra, we follow Tran et al. (1999) and use IRAF¹² routines with custom software provided by L. Simard and D. Kelson. IRAF was used to subtract the bias, remove the hot pixels, and correct the y-distortion. The spectra were then cleaned of cosmic rays using software written by L. Simard: cosmic rays were detected by determining a median value of a rectangular region surrounding each pixel and using a rejection threshold of $10\sigma_{\text{CCD}}$. This approach circumvents spurious removal of strong night sky lines.

The spectra were flat-fielded, rectified, wavelength calibrated, and sky-subtracted using Expector (Kelson 1998). Because the Tektronix CCD has severe fringing at $\lambda > 7500$ Å, multiple flat-fields were taken throughout each night; the flat-fields producing the lowest residuals were used. The wavelength solution for each slitlet was determined from the night sky lines; the list of night sky lines from Osterbrock et al. (1996) was used. The spectra were corrected for the telluric atmospheric A and B bands by using the spectrum of a bright blue star included on all the masks; the blue star also was used to roughly flux calibrate the data and remove fine structure introduced by the grating.

The 1D spectra were extracted by summing the central five rows (central $1.075''$) of each 2D spectrum. The observed wavelength coverage of the 711 targets depended on the grating and slitlet position, but was typically 6000–9500 Å. For most cluster galaxies, this includes the [OII] $\lambda 3727$ doublet and 4000 Å break as well as the H δ and H γ lines.

We refer the reader to Tran et al. (2005a) for details on how redshifts were measured using XCSAO (Kurtz et al. 1992). Typical redshift errors from the cross-correlation routine were ~ 30 km s⁻¹. However, these quoted errors tend to underestimate the true errors because they do not account for systematic uncertainties. To better quantify the errors, we compare the redshifts for 34 cluster galaxies that were observed in multiple masks. The median difference in the measured redshifts for these galaxies is 0.0003 (50 km s⁻¹).

Including serendipitous objects, the final catalog has redshifts for 433 unique objects: 31 stars, 153 cluster galaxies, and 249 field galaxies. The redshift distribution for the galaxies at $0 < z < 1$ are shown in Figure. 1. All redshifts were given a quality flag where $Q_z = 3$ denotes multiple features (“definite”), $Q_z = 2$ denotes redshifts with one strong feature and a weaker one (“probable”), and $Q_z = 1$ denotes only one feature (“estimate”). In our analysis, we consider only members with a redshift quality flag of $Q_z = 3$; this reduces the total cluster sample to 129 members, of which 121 fall on the HST/WFPC2 mosaic and 120 on the HST/ACS mosaic (Table 1). We also list the 24 galaxies that are likely to be MS1054 members but that have $Q_z = 2$ or 1 in Table 1. Redshifts for the 31 stars and 249 field galaxies will be published in Magee et al. (2007).

2.4.2. Completeness & Selection Effects

In the following discussion on completeness and selection effects, we consider only the objects that fall on the

¹² IRAF is distributed by the National Optical Astronomy Observatories, which are operated by the Association of Universities for Research in Astronomy, Inc., under cooperative agreement with the National Science Foundation.

WFPC2 mosaic because most of the spectroscopic survey was designed using the WFPC2 catalog (see §2.1). We consider the possibility of 1) magnitude bias due to the inherent difficulty of measuring redshifts for fainter objects and 2) color bias due to redshifts being more easily measured for galaxies with emission lines.

By comparing the number of galaxies in the WFPC2 photometric catalog to the number of spectroscopic targets and acquired redshifts, we investigate the completeness of our survey by following the analysis described in Yee et al. (1996). Figure 2 shows the sampling rate, success rate, and completeness of our sample as a function of I_{814} . The sampling rate, defined as the number of spectroscopic targets divided by the number of galaxies in the WFPC2 catalog, remains $> 50\%$ to $I_{814} = 22$. The success rate, defined as the number of acquired redshifts divided by the number of targets, is even higher at $\gtrsim 90\%$ to $I_{814} = 22$.

The magnitude selection function $C(m)$, also known as the completeness, is a measure of the magnitude bias and is shown in the bottom of Fig. 2. $C(m)$ is the product of the sampling and success rates, and it is defined as the number of redshifts divided by the number of galaxies in the photometric catalog. Redshifts for 8 of the 26 objects brighter than the BCG were not obtained because of a geometric bias against objects at the edges of the WFPC2 mosaic. As we focus on cluster galaxies and these eight are clearly not members, this is not a concern. Incompleteness at $I_{814} > 22.0$ is due mainly to sparse sampling rather than an inability to measure redshifts at these magnitudes; this is a common characteristic of redshift surveys (Yee et al. 1996; Fisher et al. 1998). For the cluster population, we are $> 75\%$ complete at $I_{814} \leq 21.2$ (m^* ; Hoekstra et al. 2000).

To determine if our redshift sample is biased against faint, red (passive) galaxies, we compare $(V_{606} - I_{814})$ of the galaxies in the WFPC2 catalog to the subset with measured redshifts; because this is more of a concern at fainter magnitudes, we focus on objects with $21 < I_{814} < 23$. Figure 3 shows the $(V_{606} - I_{814})$ distributions for galaxies in the WFPC2 catalog, the subset with measured redshifts, and the cluster galaxies. To remove the bias introduced by sparse sampling at fainter magnitudes, we also determine the weighted color distribution of the redshift sample $(V_{606} - I_{814})_{Wz}$. In this distribution, each galaxy is weighted by the inverse of the magnitude selection function $C(m)$. Applying the Kolmogorov-Smirnov test (Press et al. 1992) shows that $(V_{606} - I_{814})_{Wz}$ is indistinguishable from $(V_{606} - I_{814})$ for galaxies in the WFPC2 catalog. After correcting for sparse sampling, there is no measurable bias against faint, passive galaxies in our spectroscopic survey.

2.4.3. Equivalent Widths & Spectral Types

We measure the equivalent widths (EW) of [OII] λ 3727, H δ , and H γ using the same spectral bandpasses used in Fisher et al. (1998) and Tran et al. (2003a, 2005a). Although H β is included in the wavelength range for most of the cluster galaxies, in most cases it is compromised by strong sky lines. The bandpasses are based on Worthey & Ottaviani (1997), but the continuum sidebands have been moved further away from the line center because these sidebands overlap with the absorption lines

for post-starburst galaxies. In our analysis, we adopt the convention that emission lines have negative EW values and absorption lines have positive EW values.

We separate the cluster galaxies into three spectral types: 1) absorption-line members with no significant [OII] emission ($> -5\text{\AA}$) and no strong Balmer absorption $[(H\delta + H\gamma)/2 < 4\text{\AA}]$; 2) emission-line members with strong [OII] emission ($\leq -5\text{\AA}$); and 3) post-starburst (“E+A”) members that have very weak or no [OII] emission ($> -5\text{\AA}$) and strong Balmer absorption $[(H\delta + H\gamma)/2 \geq 4\text{\AA}]$. The measured equivalent widths are listed by spectral type in Table 1. Figure 4 plots [OII] versus Balmer values for 115 members (five of the 120 members with ACS imaging do not have measured [OII]).

3. CLUSTER CHARACTERISTICS

3.1. Redshift, Velocity Dispersion, & Virial Mass

In our spectroscopic catalog of 433 objects in the MS1054 field, we identify 153 galaxies with redshifts $0.80 < z < 0.86$; considering only the cluster galaxies with redshift quality flags of $Q_z = 3$ leaves 129 individual members. The cluster galaxies define a strong peak in redshift space (Fig. 1).

Using the biweight and jackknife methods (Beers et al. 1990), we measure the mean redshift and line of sight velocity dispersion of the 129 members to be $z = 0.8307 \pm 0.0004$ and $\sigma_z = 1156 \pm 82\text{ km s}^{-1}$. MS1054’s velocity dispersion and X-ray temperature ($8.6 \pm 1.1\text{ keV}$; Gioia et al. 2004) are consistent with no evolution in the $\sigma_z - T_X$ relation to $z = 0.83$.

To estimate MS1054’s virial mass, we follow Ramella et al. (1989) and first determine the cluster’s virial radius using:

$$R_V = \frac{\pi \bar{V}}{H_0} \sin \left\{ \frac{1}{2} \left[\frac{N_m(N_m - 1)}{2} \left(\sum_i \sum_{j>i} \theta_{ij}^{-1} \right)^{-1} \right] \right\} \quad (4)$$

where \bar{V} is the mean velocity of the cluster, N_m is the number of members, and θ_{ij} the angular separation between the i^{th} and j^{th} members. With R_V , we can then estimate the mass using

$$M_V = \frac{6\sigma_z^2 R_V}{G} \quad (5)$$

where σ_z is the line of sight velocity dispersion and G the gravitational constant.

Using the 129 members, MS1054’s virial radius is $1.8h^{-1}\text{ Mpc}$ ($231''$) and, using a bootstrap to resample the data-set 1000 times, we estimate the associated error to be 0.1 Mpc. The corresponding virial mass is $3.3 \times 10^{15} M_\odot$ and, adding the errors due to measuring the velocity dispersion and R_V in quadrature, the total error on the virial mass is $0.6 \times 10^{15} M_\odot$. Our result is consistent with both the weak-lensing and X-ray analyses by Jee et al. (2005): assuming a single isothermal sphere, they measure a virial radius from the ACS weak-lensing map of $1.5 \pm 0.1h^{-1}\text{ Mpc}$ and from the *Chandra* X-ray map of $1.7 \pm 0.2h^{-1}\text{ Mpc}$.

3.2. Substructure

Although MS 1054–03 falls on the $\sigma_z - T_X$ relation, it is not a virialized structure: X-ray studies have shown that the cluster contains two bright clumps, and weak-lensing analyses have revealed at least three distinct mass peaks (*e.g.* Hoekstra et al. 2000; Jeltema et al. 2001; Gioia et al. 2004; Jee et al. 2005). The spatial distribution of the confirmed members is shown in Fig. 5 where we have separated members by galaxy class. We find that the cluster galaxies trace the same elongated and clumpy structure that is seen in both the X-ray and weak-lensing mass maps; in Fig. 6, we overlay the cluster galaxies onto the ACS weak-lensing mass map from Jee et al. (2005) and the XMM-*Newton* X-ray map from Gioia et al. (2004).

To quantify the degree of substructure in MS1054, we use the Dressler-Shectman test (Dressler & Shectman 1988). By using redshifts and spatial positions, the D-S test quantifies how much the local mean redshift and velocity dispersion (as defined by the ten nearest neighbors to each galaxy) deviate from the cluster’s global values. Using biweight measures of redshift and velocity dispersion in the D-S test, we find that the degree of substructure in MS1054 is significant at the $> 95\%$ level.

4. COLOR-MAGNITUDE RELATION

The color-magnitude diagram is a powerful tool for tracing the relative (stellar) ages and the homogeneity of the different galaxy populations (*e.g.* Bower et al. 1992). In our analysis, we consider only the 120 members that lie on the ACS mosaic with redshift quality flags of 3 (see §2.4.1). This ensures that we include only the cluster galaxies with measured colors, magnitudes, and Hubble types from the ACS imaging. We group the members into the three spectral types defined in §2.4.3 as well as the three morphological types classified by P05: elliptical ($-5 \leq T \leq -3$), S0 ($-2 \leq T \leq 0$), and spiral+irregular ($T \geq 1$). The spatial distributions of the different galaxy classes are shown in Fig. 5. Of these 120 members, 115 are also assigned spectral types.

4.1. Fitting the Color-Magnitude Relation

In Fig. 7 (left panels), we show the color-magnitude (CM) diagram where the 115 (120) members are separated into the different spectral (morphological) types. Here we use the AB i_{775} magnitudes and $(V - i_{775})$ colors measured by B06. The colors are measured within a circular effective radius, and the measurement errors on the colors are $\delta(V - i_{775}) \sim 0.02$ for members brighter than $i_{775} = 22.5$ and $\delta(V - i_{775}) \sim 0.03$ for fainter members.

To fit the CM relation and determine the scatter in color, we use the absorption-line members. From Fig. 7 (left panels), we see that these members define a narrow sequence over ~ 3.5 magnitudes: their deviation from the CM relation (quantified as $\Delta(V - i_{775})$) measured by B06 is less than 0.2. To determine the CM relation defined by the red absorption-line members, we exclude the five galaxies that clearly deviate from the CM relation and use the remaining 67 absorption-line members to determine that:

$$(V - i_{775}) = 1.602 - 0.024(i_{775} - 22) \quad (6)$$

Compared to B06, who fit the CM relation using only the

ellipticals, we find a slightly flatter slope; however, this difference is within the errors (B06 quote an error of 0.014, and we estimate a comparable error). If we use only the 62 absorption-line members with $|\Delta(V - i_{775})| < 0.1$, the slope is -0.032 .

In Fig. 7 (right panels), we show the difference between the measured color and the color predicted from our fitted CM relation for the different galaxy classes. We consider $\Delta(V - i_{775}) = -0.2$ to be the division between red and blue galaxies. The measured offset and scatter in color for the different galaxy classes are listed in Table 2; the offset and scatter were determined using the biweight estimate and scale, respectively (Beers et al. 1990). Following B06, we also determine the intrinsic scatter in color (σ_{int}) by correcting for measurement errors. Included in Table 2 are the mean $(V - i_{775})$ and $(i_{775} - z_{850})$ colors, where both are also determined using the biweight estimate. The uncertainties in the offset, scatter, and colors were determined by bootstrap resampling (biweight estimate of 5000 realizations). Changing the slope, *e.g.* from -0.024 to -0.032 , has negligible impact on the measured color offsets and scatters; the differences are within the quoted errors.

At $z = 0.83$, the observed $(V - i_{775})$ and $(V - z_{850})$ colors correspond very closely to Johnson $(U - B)_z$ and $(U - V)_z$. For comparison to earlier work on Coma (Bower et al. 1992; Terlevich et al. 2001) and MS1054 (vD00), we include CM diagrams for these rest-frame colors (Fig. 8). Again we fit the CM relation using the 67 red absorption-line members:

$$(U - B)_z = 0.364 - 0.021(B_z - 22) \quad (7)$$

$$(U - V)_z = 1.232 - 0.053(V_z - 22) \quad (8)$$

The CM relation in $(U - B)_z$ is consistent with that determined by vD00 for MS1054 using WFPC2 photometry of 30 E+S0 members. As noted in §2.3, the color scatter in observed $(V - i_{775})$ is easily transformed to $(U - B)_z$ by multiplying by 0.85.

4.2. Absorption-Line Members: A Uniformly Tight Red Sequence

In our spectroscopic sample, $63 \pm 7\%$ of the members are absorption line galaxies. The absorption-line members define a strikingly narrow sequence along the CM relation: virtually all of these galaxies (67/72) have $\Delta(V - i_{775}) > -0.2$; the few that are blue are consistent with the associated error on the measured absorption-line fraction.

The intrinsic scatter in color for the absorption-line members is extremely small; it is comparable to that of the morphologically classified ellipticals ($\sigma_{Vi} = 0.048 \pm 0.009$ vs. 0.055 ± 0.008 ; Table 2). We note that most galaxy cluster surveys at $z > 0.5$ do not have the high resolution space-based imaging needed to separate ellipticals from S0s. If we consider instead the ellipticals and S0s together as a single class, their intrinsic color scatter ($\sigma_{Vi} = 0.072 \pm 0.010$) is measurably larger than that of the absorption-line members.

For the red absorption-line members, the scatter in color remains small over the observed magnitude range: it is essentially the same for both bright and faint members (Table 2). In contrast, the scatter in color for the faint red

ellipticals is $\sim 50\%$ larger than for the bright red ellipticals. In this comparison, we have excluded any absorption or elliptical members with $\Delta(V - i_{775}) < -0.2$ to ensure that the color scatter is not inflated by blue outliers.

The tightness of the CM relation for the absorption-line members demonstrates that their stellar populations are uniformly old; the intrinsic scatter in $(V - i_{775})$ corresponds to σ_{UBz} of only 0.041. Comparing this small color scatter to the mixed star formation models from van Dokkum et al. (1998) indicates that all star formation ceased by $z \sim 1.2$, and that most of these members ($> 75\%$) formed by $z \sim 2$. This is consistent with the *mean* stellar ages we estimate from their colors: comparing to the single stellar burst models (solar metallicity) in B06, their mean $(V - i_{775})$ and $(i_{775} - z_{850})$ colors correspond to mean stellar ages of ~ 3 Gyr.

In MS1054, we see that spectroscopy with even a generous color cut of $\Delta(V - i_{775}) > -0.2$ is extremely effective at identifying a homogeneously old population that follows the fitted CM relation over a factor of ~ 25 in luminosity. Our survey shows that selecting by spectral type can be better at isolating a uniformly old galaxy population than with only either color or morphological cuts, especially over a wide range in luminosity at $z > 0.8$.

4.3. Post-Starburst (E+A) Members

Post-starburst galaxies, often referred to as E+A or k+a galaxies, are galaxies where star formation has been truncated. E+As make up 5 – 20% of the galaxies in $z > 0.3$ clusters (Dressler & Gunn 1983; Couch & Sharples 1987; Dressler et al. 1999; Tran et al. 2003a), but whether the E+A phase plays an important role in the evolution of early-type members remains a point of contention (Balogh et al. 1999; Dressler et al. 2004). This is primarily because E+As can only be identified spectroscopically and, being a short-lived phenomenon ($\lesssim 1.5$ Gyr; Couch & Sharples 1987), they are relatively rare.

In MS1054, we find that the E+As make up $15 \pm 4\%$ of the cluster population; this is consistent with the fraction published in Tran et al. (2003a). An E+A spectrum can be produced via several star formation histories: while most commonly associated with a combination of a starburst that ended within the last ~ 1.5 Gyr and an older stellar population (Dressler & Gunn 1983; Couch & Sharples 1987; Barger et al. 1996; Poggianti et al. 1999), E+As can also result from continuous star formation that was truncated (Newberry et al. 1990). This combined with variations in the stellar mass produced in the most recent star formation episode leads to E+As that can span a range in *mean* stellar age, and thus the E+As should have a larger scatter in color compared to the absorption-line members.

The E+As in MS1054 have an intrinsic color scatter that is three times larger than that of the absorption-line population: $\sigma_{Vi} = 0.152 \pm 0.052$ vs. 0.048 ± 0.009 (Table 2). However, the relative age differences and corresponding scatter in color will diminish as the E+As evolve. Assuming no further star formation, the E+As observed at $z = 0.83$ ($\sigma_{UBz} = 0.129$) will lie on the CM relation and be indistinguishable from the absorption-line members by

the present epoch (*e.g.* Bower et al. 1998). Thus the current generation of E+As will increase the absorption-line fraction by a substantial amount ($\sim 15\%$).

One notable E+A is the unusually red S0 member H3910. As discussed in B06, H3910’s colors suggest that there was starburst ~ 0.5 Gyr ago and that the galaxy is currently heavily obscured by dust. This is consistent with the post-starburst nature of H3910’s spectrum. It is also possible that the dust in H3910 is obscuring any current star formation, as is observed in a handful of post-starburst galaxies in a cluster at $z = 0.41$ (Smail et al. 1999).

For the remainder of the paper, we use the terms E+A and post-starburst interchangeably. However, we recognize that there is some ambiguity given that 1) truncated star formation can also produce an E+A and 2) even if there was a burst, there is no guarantee that there will not be another one in the future. A more generic term would be post-starforming galaxy, but we use the adopted terminology to emphasize the rapid truncation in star formation that is required, regardless of the star formation history leading up to it.

4.4. Emission-Line Members

In MS1054, the emission-line members make up $23 \pm 4\%$ of the cluster population and they tend to have bluer colors than both the absorption-line and E+A members. However, not all of the emission-line members are blue: 7/26 have $\Delta(V - i_{775}) > -0.2$. In addition, all of these red emission-line members are fainter than $i_{775} = 22$ and have early-type morphologies. We note that a similar population of emission-line, red, early-type members also has been found in Cl0152 ($z = 0.837$; Homeier et al. 2005). Color cuts, even when combined with morphological classifications, cannot separate emission from absorption-line members, especially at fainter luminosities.

The emission-line members have the largest color offset and scatter of all the galaxy classes; their color scatter is even larger than that of the morphologically classified Sp+Irr members (0.407 ± 0.064 vs. 0.273 ± 0.065). Comparing their mean colors (Table 2) to the solar metallicity models from B06 indicates that a typical emission-line member is $\sim 1.5 - 2$ Gyr younger than the absorption-line members and has had some combination of continuous or bursting star formation. Most of these galaxies ($> 75\%$) will fade into faint ($L < L^*$) members. This is supported by their internal velocity dispersions ($\propto \text{mass}$): $\sim 80\%$ of the emission-line members have estimated internal velocity dispersions¹³ of $< 100 \text{ km s}^{-1}$ (Fig. 9). Assuming they evolve into low-mass early-type members, their younger mean stellar ages relative to the more massive early-types are consistent with trends observed in lower redshift clusters, *e.g.* Coma and Abell 2218 (Poggianti et al. 2001; Smail et al. 2001).

4.5. The Morphological Types: Elliptical, S0, & Spiral+Irregular Members

Using the morphological types assigned by P05, we find that the ellipticals in MS1054 define a tight red sequence that is comparable to that of the absorption-line members

¹³ Following Tran et al. (2003b), we use measured internal velocity dispersions (σ_{1D}) for 27 of the members (errors $< 50 \text{ km s}^{-1}$; Wuyts et al. 2004) and estimated σ_{1D} for the remainder.

(Fig. 7; Table 2). In comparison, the intrinsic color scatter for the S0s is twice that of both the ellipticals and the absorption-line members (Table 2); this is true even if we compare only the brightest ($i_{775} \leq 22$) S0s to the brightest ellipticals and absorption-line members. However, the increased color scatter for the S0 sample is primarily due to a small fraction of blue S0s; most of the S0s (28/39; 72%) are as red as the ellipticals and absorption-line members. If we consider only members with $\Delta(V - i_{775}) > -0.1$, the intrinsic color scatter for the absorption-line, elliptical, and S0 samples are comparable: 0.044 ± 0.011 , 0.040 ± 0.011 , and 0.047 ± 0.018 , respectively.

The differences in the color scatters indicate that, on average, the ellipticals are more uniform in age than the S0s. Dust can also play a role by making some of the S0s redder (as in the case of H3910; see §4.3); dust would decrease the mean color offset for the S0s, but the S0s would still retain a larger color scatter. Unlike the ellipticals, a number of the S0s are blue (7/39; 18%) and/or are post-starburst systems (8/39; 21%); this suggests that the S0s and ellipticals are not drawn from the same parent population. We return to this issue in §5.

Note that all seven of the blue S0s are fainter than $i_{775} = 22$; assuming these S0s will evolve onto the red sequence at $z < 0.8$, they will remain $L < L^*$ members. The resulting younger mean ages for the faint S0s is consistent with the difference in mean age between the bright ellipticals and faint S0s in Coma (Poggianti et al. 2001).

As reported in vD00, the Spiral+Irregular members have the largest color offset and scatter of the morphological classes (Table 2). However, several of the bright Sp+Irr are red and considered to be absorption-line or post-starburst systems (see Fig. 7). Again we see that the combination of color and morphology does not consistently correspond to recent star formation: many of the Sp+Irr members are red and/or absorption-line systems, and vice versa for the S0 members.

4.6. Color Scatter in Rest-frame Johnson Filters

In our analysis, we prefer to use observed ACS colors to preserve the model-independence of our results. However, we include rest-frame Johnson colors so that we can compare to the color scatter measured in, *e.g.* Coma. In Table 3, we list the mean color offset and color scatter in $(U - V)_z$ for the galaxy classes. As described earlier, the CM relation is fitted to the 67 red absorption-line members.

The differences in the $(U - V)_z$ offset and scatter between the galaxy classes are consistent with our earlier results using observed $(V - i_{775})$: the absorption-line members define the tightest red sequence with an intrinsic $\sigma_{UVz} = 0.083 \pm 0.012$. The elliptical-only sample also has a small $(U - V)_z$ scatter of 0.087 ± 0.015 . In comparison, the S0-only sample has a color scatter that is nearly twice as large ($\sigma_{UVz} = 0.187 \pm 0.063$); this increases the $(U - V)_z$ scatter for the E+S0 population as a whole to 0.110 ± 0.020 . However, we again note that the larger S0 scatter is mainly due to a number of S0s ($\sim 20\%$) that are blue, and that most of the S0s are as red (old) as the elliptical and absorption-line members (see Fig. 8).

The absorption-line members in MS1054 have an intrinsic $(U - V)_z$ scatter that is more than twice as

large as that of the Coma ellipticals ($\sigma_{UV} = 0.036 \pm 0.020$; Terlevich et al. 2001). If the current generation of absorption-line members in MS1054 continue to evolve passively, their $(U - V)_z$ scatter will decrease considerably over the next ~ 7 Gyr, the look-back time to $z = 0.83$. Comparing to the mixed star formation models from van Dokkum et al. (1998), we see that in models where all activity ceases by $z \sim 1.2$ the color scatter decreases by approximately a factor of three between $z \sim 0.8$ and $z \sim 0$. Thus by $z \sim 0$, the absorption-line members in MS1054 will have as small a color scatter as the Coma ellipticals. This decrease in the $(U - V)$ scatter is also consistent with the mixed star formation histories for Coma modeled by Bower et al. (1998). The absorption-line galaxies in MS1054 will evolve into the oldest members of local clusters.

5. COMPOSITE CLUSTER SPECTRA

To investigate the global properties of the cluster population, we combine the spectra of the 120 members by galaxy type. We first normalize each 1D spectrum to unity over rest-frame 4200 – 4600Å and then take an average because we are interested in a representative spectrum for each galaxy type. We then remove spuriously high pixel values due to, *e.g.* contamination by sky lines, by smoothing the average spectrum using a large window, subtracting this smoothed spectrum, and removing pixel values that are 30% larger. The composite spectra for the spectral and morphological classes are shown in Fig. 10.

For each composite spectrum, we measure the same spectral indices defined in §2.4.3. We determine errors by bootstrapping 1000 realizations for each galaxy class using the base set, and then measuring the same indices in the generated composite spectra; the error is the biweight scale of the resulting distribution divided by $\sqrt{N_g}$.

As part of our analysis, we also measure $H\delta_A$ and $D_N(4000)$ using the bandpasses defined in Kauffmann et al. (2003, hereafter K03). $H\delta_A$ and $D_N(4000)$ were developed by K03 as a method to detect starbursts that occurred within the past 1 – 2 Gyr and thus better quantify the star formation histories of the local galaxies in the Sloan survey. With our composite spectra, we can robustly measure both of these spectral diagnostics and compare them directly to K03's library of different star formation histories generated using Bruzual & Charlot (2003, hereafter BC03) models. We list the measured spectral indices in Table 4.

5.1. The Spectral Types: Absorption-line, Post-Starburst, & Emission-line

In Fig. 10 (top), we show the composite spectra for the absorption-line, post-starburst (E+A), and emission-line members. The composite spectra have the features that are typically associated with the different types: the absorption-line spectrum has the strong G-band absorption that results from a stellar population dominated by F and G type stars (*e.g.* see Gunn & Stryker 1983); the E+A spectrum is similar to the absorption-line one, but with stronger $H\delta$ and $H\gamma$ absorption due to more recent star formation (< 2 Gyr); and the emission-line spectrum shows [OII] emission that presumably is associated with current star formation.

Using the Sloan survey, Dressler et al. (2004) showed that the strong $H\delta$ absorption coupled with no [OII] emission observed in distant clusters cannot be reproduced by a mix of local star formation histories, *i.e.* by star formation that is quenched over long (> 1 Gyr) timescales. Rather, more intense star formation such as bursts are required. Given their strong Balmer absorption, we expect such a starburst phase for the E+As. The emission-line members also show strong Balmer absorption indicative of a recent spate of star formation in addition to the current level of activity. Even the absorption-line members have weak $H\delta_A$ absorption ($\sim 0.5\text{\AA}$), a value consistent with a mean stellar age of ~ 2.8 Gyr (KC03).

5.2. The Morphological Types: Elliptical, S0, & Spiral-Irregular

In Fig. 10 (bottom), we show composite spectra for the combined early-type sample as well as for the elliptical, S0, and Spiral+Irregular members. The combined early-type sample shows $H\delta$ absorption that is measurably stronger than in the absorption-line spectrum ($H\delta = 2.5$ vs. 1.7; Table 4). Assuming that the stronger $H\delta$ absorption is due to more recent star formation, the morphologically classified E+S0 members are not as homogeneously old as the absorption-line population.

Because the ACS imaging allows us to separate the ellipticals and S0s, we can compare their individual composite spectra to search for any differences in their mean stellar populations, *i.e.* any trends introduced by the blue S0s (see §4). Note that K-S tests confirm the ellipticals and S0s have indistinguishable i_{775} and σ_{1D} distributions, *i.e.* any differences between the two composite spectra are unlikely to be due to other factors such as the mass-metallicity relation.

The $H\delta_A$ absorption in the S0s is nearly 2\AA stronger and their $D_N(4000)$ index lower than in the ellipticals. Surprisingly, the S0 spectrum also shows weak [OII] emission, a sign of ongoing star formation. These differences are consistent with the larger scatter in color exhibited by the S0s compared to the ellipticals (§4; Table 2), and are due mostly to the S0s that are blue (7/39; 18%). Comparing $H\delta_A$ and $D_N(4000)$ to the single burst model (solar metallicity; KC03) shows an age difference of $\sim 0.5 - 1$ Gyr.

Is there still a difference between the ellipticals and S0s if we exclude the seven faint, blue S0s? To test this, we generate composite spectra for the bright, red ellipticals and S0s ($i_{775} \leq 22$; $\Delta(V - i_{775}) \geq -0.2$; Table 4). The mean luminosities of both sets are identical ($i_{775} = 21.4$), thus we can be sure that any differences in the spectral indices are not due to a luminosity effect.

A surprisingly high fraction (30%; 4/13) of the bright, red S0s are post-starburst systems. This leads to the composite S0 spectrum having both stronger $H\delta_A$ absorption and lower $D_N(4000)$ than the composite spectrum of the bright, red ellipticals. Because $H\delta_A$ is a more sensitive tracer of relative age than $D_N(4000)$ in the range of mean stellar ages probed here (1–3 Gyr; K03), we use $H\delta_A$ and estimate an age difference of ~ 0.5 Gyr. Thus even the composite spectrum of the bright, red S0s corresponds to a younger mean age than that of the bright, red ellipticals.

In concert, these results indicate that on average, the

S0s are younger (by $\sim 0.5 - 1$ Gyr) and less homogeneous in age than the ellipticals; this age difference is consistent with the measured color offset between S0 and elliptical galaxies in a cluster at $z = 1.106$ ($\Delta t \sim 1$ Gyr; Mei et al. 2006). However, we note that even a difference in age of 1 Gyr at $z = 0.8$ will have faded and not be detectable by the current epoch, *i.e.* 7 Gyr later.

Although separating ellipticals from S0s is challenging and there is usually considerable contamination between the two types, we find that the ellipticals and S0s in MS1054 are not drawn from the same parent population: while many of the S0s are as old as the ellipticals, there are a number of S0s that are blue (18%) and/or have a post-starburst signature (21%). Our results confirm that an average elliptical in MS1054 is younger than an average S0, and that it is possible to reliably separate ellipticals and S0s at $z = 0.83$ with high resolution imaging ($\sim 0.4h^{-1}$ kpc).

5.3. Red Mergers

For completeness, we include a brief analysis of the members that are in red, merging systems. MS1054's unusually high fraction of red galaxy-galaxy mergers ($\sim 17\%$) was first reported by van Dokkum et al. (1999) and later spectroscopically confirmed by Tran et al. (2005a). The composite spectrum of the 17 red merging members from Tran et al. (2005a) is included in Fig. 10 (bottom), and the corresponding spectral indices listed in Table 4. The red merger spectrum is essentially identical to both the composite absorption-line and elliptical spectrum, and it has similar values for $H\delta_A$ and $D_N(4000)$. These spectral diagnostics reinforce our previous conclusions that the galaxies in these red, merging systems are dominated by an old stellar population with no ongoing star formation, and that most of the massive galaxies in MS1054 evolved from dissipationless mergers.

5.4. $H\delta_A$ vs. $D_N(4000)$: Comparing Star Formation Histories

In Fig. 11, we plot $H\delta_A - D_N(4000)$ for the different spectral and morphological types; the figure also includes the models, both for mixed star formation histories (dots) and a single burst (curve), from K03. The mixed star formation histories include combinations of continuous star formation with random bursts of varying strength. To zeroth order, $D_N(4000)$ traces the mass-to-light ratio such that galaxies with larger (M/L) ratios, *i.e.* those dominated by older stars, have higher $D_N(4000)$ indices. However, at fixed $D_N(4000)$, galaxies with stronger $H\delta_A$ absorption have a higher fraction of young stars and therefore smaller (M/L) ratios. Combining $D_N(4000)$ with $H\delta_A$ thus enables us to better gauge whether a galaxy has experienced a burst within the last 2 Gyr, and whether this recent episode increased the stellar mass significantly.

Immediately apparent from the top panel of Fig. 11 is that the recent (< 1.5 Gyr) star formation histories of the absorption-line, post-starburst, and emission-line members are very different. Assuming solar metallicity, we find that the indices for the composite absorption-line spectrum are consistent with a single starburst that is ~ 2.8 Gyr old ($z_f \sim 1.8$). The indices for the composite post-starburst spectrum are also consistent with a single

starburst, but one that is only ~ 1.6 Gyr old ($z_f \sim 1.2$). In comparison, the indices for the emission-line spectrum differ from a single starburst and indicate a continuous and/or bursting star formation history (see K03) where the mean stellar age is ~ 0.4 Gyr ($z_f \sim 0.9$).

Fig. 11 also shows $H\delta_A - D_N(4000)$ for the morphological types (bottom panel). The composite elliptical spectrum has $H\delta_A$ and $D_N(4000)$ values comparable to those of the absorption-line spectrum. This mirrors the result from their colors that the elliptical and absorption-line galaxies are the oldest members (see §4). In comparison, the S0s have stronger $H\delta_A$ absorption and lower $D_N(4000)$, consistent with our conclusion that the S0s have had more recent star formation and are not as uniformly old as the absorption-line members.

The $H\delta_A - D_N(4000)$ values of the composite absorption-line spectrum confirm that these are the oldest galaxies in MS1054, a result that is consistent with their small scatter in color (see §4); only stellar populations (solar metallicity) with mean ages > 2.5 Gyr can have $D_N(4000) > 1.65$ and $H\delta_A \lesssim 0.5\text{\AA}$ (K03). Using $H\delta_A - D_N(4000)$ reinforces our conclusion that selecting by spectral type alone is most effective at isolating a homogeneously old population.

6. SIGNS OF AGE ON THE RED SEQUENCE: GALAXY COLOR & $H\delta$ ABSORPTION

With our spectral survey, we are able to identify a uniformly old population of galaxies in MS1054: in terms of both their spectral and photometric properties, the absorption-line members are older and more homogeneous in mean stellar age than the post-starburst, emission-line, and morphologically classified E+S0 members. The absorption-line members make up 63% of the current cluster population, span a wide range in luminosity (factor of 25), and have a small scatter in color. Spectral diagnostics show that the composite absorption-line member has a mean stellar age of ~ 2.8 Gyr ($z_f \sim 1.8$).

However, many of the cluster galaxies continue to evolve in color, morphology, and spectral line strength, *i.e.* the red sequence continues to assemble. A significant fraction ($\sim 15\%$) of MS1054's members are post-starburst systems that are likely to evolve into absorption-line members, and there are a number of spectroscopically confirmed red mergers that can only evolve into massive, passive members (van Dokkum et al. 1999; Tran et al. 2005a). In the following, we compare different subsets of the cluster galaxies to further illustrate how the red sequence in MS1054 has evolved since $z \sim 1.8$, and how it continues to be populated at $z < 0.83$.

6.1. A Correlation Between $H\delta_A$ & Color Offset

To test for variations in relative age between the absorption-line population and other members on the red sequence, *e.g.* the E+As, we consider how the $H\delta_A$ equivalent width varies as a function of offset in $(V - i_{775})$ for the cluster galaxies. Because there may be a trend in $H\delta_A$ with magnitude due to, *e.g.* the metallicity-luminosity relation (Gallazzi et al. 2006), we normalize $H\delta_A$ by subtracting from the measured $H\delta$ EW the $H\delta_A - i_{775}$ relation where the latter is determined by a least-squares fit to the red absorption-line members:

$$H\delta_A = 0.047 - 1.670(i_{775} - 22) \quad (9)$$

We note that this trend between $H\delta_A$ and i_{775} is not statistically significant using a Spearman rank test. However, we use the normalized $H\delta$, hereafter referred to as $\Delta H\delta_A$, to ensure the robustness of our results.

Fig. 12 (right panels) highlights the impressively tight color distribution of the absorption-line population: 92% (66/72) of the absorption-line members have $\Delta(V - i_{775}) > -0.1$. The ellipticals also show a tight color distribution with 89% (49/55) having $\Delta(V - i_{775}) > -0.1$. In comparison, only 72% (28/39) of the S0s are as red.

Fig. 12 (left panels) reveals that even on the red sequence, there is a trend between color deviation and $H\delta_A$ absorption. We fit a least squares to $\Delta H\delta_A$ vs. $\Delta(V - i_{775})$ for all of the members with $-0.2 \leq \Delta(V - i_{775}) \leq 0.2$ and $\sigma_{1D} > 150 \text{ km s}^{-1}$; the lower limit on the internal velocity dispersion provides a mass-limited sample and ensures that we are not introducing a luminosity bias into the fit. With these 52 members, we find that:

$$\Delta H\delta_A = 1.13 - 19.93\Delta(V - i_{775}) \quad (10)$$

The Spearman rank test (Press et al. 1992) confirms that the trend of weakening $H\delta$ absorption with redder colors is significant with $> 95\%$ confidence. In terms of how large the age variations are for such a relatively small difference in color, we note that a member with $(V - i_{775}) = 1.6$ is older than a member with $(V - i_{775}) = 1.5$ by ~ 1 Gyr; this is determined by comparing the corresponding $(U - B)_z$ values of 0.35 and 0.27 to a BC03 single burst model (solar metallicity; B06).

Assuming that the observed trend between weakening $H\delta_A$ absorption and redder colors is due to differences in mean stellar age implies that even amongst the absorption-line members, there is a trend in age with color. To test whether this is the case, we separate the red absorption-line members into two smaller bins that straddle $\Delta(V - i_{775}) = 0$ [bin size of $\Delta(V - i_{775}) = 0.1$]. We generate composite spectra for these two subsets and measure their spectral indices (Table 4).

The composite spectrum for the absorption-line members that are redder than the CM relation [$0 \leq \Delta(V - i_{775}) \leq 0.1$; 36 members] has an $H\delta_A$ EW of 0.1\AA (essentially none) and $D_N(4000) = 1.73$ (the highest value for any composite spectrum). If we use color, $H\delta_A$, and $D_N(4000)$ as proxies for mean stellar age, this would imply that 1) the absorption-line members with colors that are redder than the fitted CM relation are the oldest members and 2) any absorption-line members with more recent star formation will consequently be bluer and have stronger $H\delta_A$ absorption as well as a lower $D_N(4000)$ index. We see this is exactly the case in MS1054: the composite spectrum for the absorption-line members that are bluer than the CM relation [$-0.1 \leq \Delta(V - i_{775}) < 0$; 25 members] has a measurably stronger $H\delta_A$ EW of 1.0\AA and lower $D_N(4000)$ of 1.66. Equally remarkable is that the adjacent color bin [$-0.2 \leq \Delta(V - i_{775}) < -0.1$] is dominated by post-starburst members and thus has even stronger $H\delta_A$ absorption (Fig. 12).

6.2. Explaining the Correlation: Age vs. Metallicity

While the correlation between redder colors and weakening $H\delta_A$ absorption can result from variations in either age or metallicity (Terlevich et al. 1999), our observations indicate that age is the underlying cause because: 1) The i_{775} magnitude distributions of the absorption-line members in the two color bins are indistinguishable (K-S test), thus we are not inadvertently dividing the members into high/low metallicity groups corresponding to bright/faint members; 2) As a precaution, we have already removed any possible trend of $H\delta_A$ with magnitude by subtracting the $H\delta_A - i_{775}$ relation from the measured value; and 3) Most compelling is that of the 10 members with $-0.2 \leq \Delta(V - i_{775}) < -0.1$, six are post-starburst systems and two have strong Balmer absorption and only weak (O[II] $\sim 5 - 7\text{\AA}$) emission, meaning they too experienced a recent starburst. If the trend between $H\delta_A$ and color is due to metallicity rather than age, one would not expect this color bin to be dominated by post-starburst systems, *i.e.* galaxies that definitely have younger mean stellar ages.

To further test our hypothesis that the observed trend between $H\delta_A$ and color offset is due to variations in age, we compare our results to two simple models: Case 1) assuming a constant age of 3 Gyr and allowing the metallicity to change from $Z = Z_\odot$ at $B_z = 20$ to $Z = 0.2Z_\odot$ at $B_z = 24$; and Case 2) assuming constant solar metallicity and allowing the age to change from 3 Gyr at $B_z = 20$ to 1.4 Gyr at $B_z = 24$. We use the BC03 models with the Padova 1994 evolutionary tracks and the Chabrier initial mass function to fit the following relations for Case 1:

$$H\delta_A = -0.075 + 0.640(B_z - 20) \quad (11)$$

$$\Delta(V - i_{775}) = -0.055(B_z - 20) \quad (12)$$

and for Case 2:

$$H\delta_A = -0.075 + 0.959(B_z - 20) \quad (13)$$

$$\Delta(V - i_{775}) = -0.047(B_z - 20) \quad (14)$$

Figure 13 shows how the $H\delta_A$ absorption and color offset vary for the two models. Both models show similar trends of weakening $H\delta_A$ absorption with redder colors. However, the observed trend is best matched by Case 2 where metallicity is constant ($Z = Z_\odot$) and age varies (1.4 – 3 Gyr). For Case 1, it is possible to steepen the $H\delta_A - \Delta(V - i_{775})$ trend to better match the data, but this would require metallicities significantly lower ($\lesssim 0.2Z_\odot$) than that measured for early-type galaxies in the local universe ($Z = 0.8 - 1.6Z_\odot$; Gallazzi et al. 2006).

We have presented several lines of evidence supporting a trend between $H\delta_A$ and color offset that is due to age variations alone. However, we acknowledge that we cannot exclude metallicity as the underlying cause, either in part or in full, at a statistically robust level. For example, the least-squares fit defined by the reddest [$\Delta(V - i_{775}) \geq -0.1$] members has a slightly flatter slope ($m = -16.94$) and thus does not deviate as strongly from Case 1. Only by measuring the spectral indices needed to disentangle age and metallicity can this issue be fully resolved; such an analysis is beyond the scope of this paper.

6.3. Estimating the Age Variations on the Red Sequence

We conclude that the color scatter in MS1054’s red sequence is driven by differences in mean stellar age. To estimate the age difference bracketed by the oldest and youngest average red sequence member at $z = 0.83$, we use the $H\delta_A$ and $D_N(4000)$ values from the composite spectra of the reddest absorption-line members and the E+As (Table 4). For the $\Delta(V - i_{775}) > 0$ absorption-line spectrum, comparing both diagnostics to the single burst model (K03) shows that they have a mean age of ~ 3 Gyr while the E+As have a mean age of ~ 1.6 Gyr. Assuming no future star formation, the current population of E+As will evolve into absorption-line members that lie on the red sequence in < 2 Gyr (Barger et al. 1996). Both van Dokkum et al. (1998) and Bower et al. (1998) confirm using mixed star formation models that color scatter decreases rapidly as long as most of the members ($> 75\%$) formed at higher redshifts ($z \gtrsim 2$). Considering the large lookback time to $z = 0.83$ (7 Gyr), the larger color scatter introduced by the E+As will decrease and be indistinguishable from that of the absorption-line members by the present epoch.

7. SUMMARY & CONCLUSIONS

We present an extensive spectroscopic survey of MS 1054–03 using observations collected with Keck/LRIS. From our magnitude limited survey, we isolate 129 ($Q_z = 3$) cluster galaxies and measure MS1054’s redshift and velocity dispersion to be $z = 0.8307 \pm 0.0004$ and $\sigma_z = 1156 \pm 82 \text{ km s}^{-1}$. We estimate MS1054’s virial radius and mass to be $1.8 \pm 0.1 h^{-1} \text{ Mpc}$ and $3.3 \pm 0.6 \times 10^{15} M_\odot$, but note that the cluster has a significant amount of substructure. The absorption-line, post-starburst (E+A), and emission-line galaxies make up $63 \pm 7\%$, $15 \pm 4\%$, and $23 \pm 4\%$ of the cluster population, respectively.

Combining our spectroscopy with magnitudes, colors, and Hubble types from HST/ACS imaging (Postman et al. 2005; Blakeslee et al. 2006), we compare the different galaxy classes. In the color-magnitude diagram, the absorption-line members define a tight red sequence over a span of ~ 3.5 magnitudes: their intrinsic scatter in $(V - i_{775})$ color is only 0.048 ± 0.009 , corresponding to a scatter in Johnson $(U - B)_z$ of 0.041. The color scatter for the absorption-line members is comparable to that of the morphologically classified ellipticals ($\sigma_{Vi} = 0.055 \pm 0.008$), but it is measurably smaller than that of the combined E+S0 sample ($\sigma_{Vi} = 0.072 \pm 0.010$). Our survey demonstrates that spectroscopy is extremely effective at identifying a homogeneously old population over a wide range in luminosity ($L \gtrsim 0.5L^*$), especially at $z \gtrsim 0.8$ where visually separating ellipticals and S0s becomes quite challenging.

In MS1054, the scatter in $(U - V)_z$ for both the absorption-line and elliptical members is more than twice that of the ellipticals in Coma: $\sigma_{UVz} = 0.091 \pm 0.009$ vs. $\sigma_{UVz} = 0.036 \pm 0.020$. The difference in the color scatter is consistent with passive evolution of a population where most of the absorption-line members ($> 75\%$) formed by $z \sim 2$ (van Dokkum et al. 1998; Bower et al. 1998), and all of them by $z \sim 1.2$. The absorption-line galaxies in MS1054 are likely to evolve into the oldest members of local clusters such as Coma.

Our analysis indicates that the color scatter on the red

sequence in MS1054 is due to differences in mean stellar age. Considering only red [$\Delta(V - i_{775}) > -0.2$] members, we find a trend ($> 95\%$ confidence) between weakening H δ absorption and redder colors that we conclude is due to age. We estimate that red sequence members differ in mean stellar age by up to ~ 1.5 Gyr. However, such a difference in mean age and the resulting increase in color scatter are both negligible by the present epoch given the lookback time to $z = 0.83$ of ~ 7 Gyr.

The current generation of transitional members, *e.g.* the E+As and red mergers, include luminous/massive galaxies that will populate the red sequence across a wide range in luminosity. However, assuming that the red sequence continues to acquire more members at $z < 0.83$ as blue members fade and redden, we note that these later additions to the red sequence will be mostly faint ($L < L^*$), low-mass ($\sigma_{1D} < 100 \text{ km s}^{-1}$) members. The current deficit of morphologically classified ellipticals and S0s in particular suggests that most of these later additions to the red sequence will evolve into S0s (Tran et al. 2005a; Postman et al. 2005; Holden et al. 2006). This would result in a difference in mean stellar age between the bright ellipticals and the faint S0s, but such a difference is observed in lower redshift clusters, *e.g.* Coma (Poggianti et al. 2001).

Lastly, we generate composite spectra for the different galaxy classes and measure their spectral indices, *e.g.* H δ_A and $D_N(4000)$. Both color and spectral indices confirm that the composite absorption-line spectrum has the old-

est mean stellar population (~ 3 Gyr), and that the composite elliptical spectrum is equally as old. Remarkably, the spectral diagnostics also indicate that the composite S0 spectrum is $\sim 0.5 - 1$ Gyr younger than the composite elliptical spectrum. This is due to the fact that while most of the S0s are as red (old) as the ellipticals, $\sim 18\%$ are blue and $\sim 21\%$ are also post-starburst systems. The difference in mean stellar age between an average elliptical and S0 in MS1054 is consistent with the age difference implied by the color offset observed between ellipticals and S0s in a cluster at $z = 1.106$ (Mei et al. 2006). Although there is likely to be some mixing when separating ellipticals and S0s, our results show that at least in MS1054 at $z = 0.83$, the average elliptical is measurably older than the average S0 member.

It is a pleasure to thank G. Kauffmann for providing her star formation models, M. Jee for his weak-lensing map of MS1054, and I. Gioia for her X-ray map of MS1054. K. Tran acknowledges support from the NSF Astronomy & Astrophysics Postdoctoral fellowship under award AST-0502156 and from the NOVA fellowship program; she also thanks S. Trager for technical help with the star formation models. ACS was developed under NASA contract NAS5-32865, and this research was supported under NASA grant NAG5-7697. Finally, the authors extend special thanks to those of Hawaiian ancestry on whose sacred mountain we are privileged to be guests.

REFERENCES

- Balogh, M. L., Morris, S. L., Yee, H. K. C., Carlberg, R. G., & Ellingson, E. 1999, *ApJ*, 527, 54
- Barger, A. J., Aragon-Salamanca, A., Ellis, R. S., Couch, W. J., Smail, I., & Sharples, R. M. 1996, *MNRAS*, 279, 1
- Baugh, C. M., Cole, S., & Frenk, C. S. 1996, *MNRAS*, 283, 1361
- Beers, T. C., Flynn, K., & Gebhardt, K. 1990, *AJ*, 100, 32
- Bertin, E. & Arnouts, S. 1996, *A&A*, 117, 393
- Blakeslee, J. P., Holden, B. P., Franx, M., Rosati, P., & et al. 2006, *ApJ*
- Bower, R. G., Kodama, T., & Terlevich, A. 1998, *MNRAS*, 299, 1193
- Bower, R. G., Lucey, J. R., & Ellis, R. S. 1992, *MNRAS*, 254, 601+
- Bruzual, G. & Charlot, S. 2003, *MNRAS*, 344, 1000
- Butcher, H. & Oemler, A. 1984, *ApJ*, 285, 426
- Couch, W. J. & Sharples, R. M. 1987, *MNRAS*, 229, 423
- Diaferio, A., Kauffmann, G., Balogh, M. L., White, S. D. M., Schade, D., & Ellingson, E. 2001, *MNRAS*, 323, 999
- Donahue, D., Voit, G., Gioia, I., Luppino, G., Hughes, J. P., & Stocke, J. T. 1998, *ApJ*, 502, 550
- Dressler, A. & Gunn, J. E. 1983, *ApJ*, 270, 7
- Dressler, A., Oemler, A. J., Couch, W. J., Smail, I., Ellis, R. S., Barger, A., Butcher, H., Poggianti, B. M., & Sharples, R. M. 1997, *ApJ*, 490, 577
- Dressler, A., Oemler, A. J., Poggianti, B. M., Smail, I., Trager, S., Shectman, S. A., Couch, W. J., & Ellis, R. S. 2004, *ApJ*, 617, 867
- Dressler, A. & Shectman, S. A. 1988, *AJ*, 95, 985
- Dressler, A., Smail, I., Poggianti, B. M., Butcher, H., Couch, W. J., Ellis, R. S., & Oemler, A. J. 1999, *ApJS*, 122, 51
- Ellingson, E., Lin, H., Yee, H. K. C., & Carlberg, R. G. 2001, *ApJ*, 547, 609
- Ellis, R. S., Smail, I., Dressler, A., Couch, W. J., Oemler, A. J., Butcher, H., & Sharples, R. M. 1997, *ApJ*, 483, 582
- Fisher, D., Fabricant, D., Franx, M., & van Dokkum, P. 1998, *ApJ*, 498, 195+
- Ford, H. C., Bartko, F., Bely, P. Y., Broadhurst, T., Burrows, C. J., Cheng, E. S., Clampin, M., & et al. 1998, in *Proc. SPIE Vol. 3356*, p. 234-248, *Space Telescopes and Instruments V*, Pierre Y. Bely, James B. Breckinridge, Eds., ed. P. Y. Bely & J. B. Breckinridge, 234-248
- Gallazzi, A., Charlot, S., Brinchmann, J., & White, S. D. M. 2006, *MNRAS*, 370, 1106
- Gioia, I. M., Braito, V., Branchesi, M., Della Ceca, R., Maccacaro, T., & Tran, K.-V. 2004, *A&A*, 419, 517
- Gioia, I. M. & Luppino, G. A. 1994, *ApJS*, 94, 583
- Goto, T., Postman, M., Cross, N. J. G., Illingworth, G. D., Tran, K., Magee, D., & Franx, M. 2005, *ApJ*, 621, 188
- Gunn, J. E. & Stryker, L. L. 1983, *ApJS*, 52, 121
- Hoekstra, H., Franx, M., & Kuijken, K. 2000, *ApJ*, 532, 88
- Holden, B. P., Franx, M., Illingworth, G. D., Postman, M., Blakeslee, J. P., Homeier, N., Demarco, R., Ford, H. C., Rosati, P., Kelson, D. D., & Tran, K.-V. H. 2006, *ApJ*, 642, L123
- Homeier, N. L., Demarco, R., Rosati, P., Postman, M., Blakeslee, J. P., Bouwens, R. J., Bradley, L. D., & many more authors. 2005, *ApJ*, 621, 651
- Jee, M. J., White, R. L., Ford, H. C., Blakeslee, J. P., Illingworth, G. D., Coe, D. A., & Tran, K.-V. H. 2005, *ApJ*, 634, 813
- Jeltema, T. E., Canizares, C. R., Bautz, M. W., Malm, M. R., Donahue, M., & Garmire, G. P. 2001, *ApJ*, 562, 124
- Jørgensen, I., Franx, M., Hjorth, J., & van Dokkum, P. G. 1999, *MNRAS*, 308, 833
- Kauffmann, G. 1995, *MNRAS*, 274, 153
- Kauffmann, G., Heckman, T. M., White, S. D. M., Charlot, S., & et al. 2003, *MNRAS*, 341, 33
- Kelson, D. D. 1998, Ph.D. thesis, University of California at Santa Cruz (Santa Cruz, CA: University of California)
- Kelson, D. D., Illingworth, G. D., van Dokkum, P. G., & Franx, M. 2000, *ApJ*, 531, 184
- Kodama, T., Arimoto, N., Barger, A. J., & Arag'on-Salamanca, A. 1998, *A&A*, 334, 99
- Kurtz, M. J., Mink, D. J., Wyatt, W. F., Fabricant, D. G., Torres, G., Kriss, G. A., & Tonry, J. L. 1992, in *Astronomical Data Analysis Software and Systems I*, ed. d. M. Worrall, C. Biemesderfer, & J. Barnes, Vol. 25 (A.S.P. Conference Series), 432
- Lubin, L. M., Oke, J. B., & Postman, M. 2002, *AJ*, 124, 1905
- Mei, S., Blakeslee, J. P., Stanford, S. A., Holden, B. P., Rosati, P., Strazzullo, V., Homeier, N., & et al. 2006, *ApJ*, 639, 81
- Newberry, M. V., Boroson, T. A., & Kirshner, R. P. 1990, *ApJ*, 350, 585
- Oke, J. B., Cohen, J. G., Carr, M., Cromer, J., Dingizian, A., Harris, F. H., Labrecque, S., Luciano, R., Schaal, W., Epps, H., & Miller, J. 1995, *PASP*, 107, 375
- Osterbrock, D. E., Fulbright, J. P., Martel, A. R., Keane, M. J., Trager, S. C., & Basri, G. 1996, *PASP*, 108, 277+
- Peebles, P. J. E. 1970, *AJ*, 75, 13

- Poggianti, B. M., Bridges, T. J., Carter, D., Mobasher, B., Doi, M., Iye, M., Kashikawa, N., Komiyama, Y., Okamura, S., Sekiguchi, M., Shimasaku, K., Yagi, M., & Yasuda, N. 2001, *ApJ*, 563, 118
- Poggianti, B. M., Smail, I., Dressler, A., Couch, W. J., Barger, A. J., Butcher, H., Ellis, R. S., & Oemler, A. J. 1999, *ApJ*, 518, 576
- Postman, M., Franx, M., Cross, N. J. G., Holden, B., Ford, H. C., Illingworth, G. D., & et al. 2005, *ApJ*, 623, 721
- Press, W. H., Teukolsky, S. A., Vetterling, W. T., & Flannery, B. P. 1992, *Numerical recipes in FORTRAN. The art of scientific computing* (Cambridge: University Press, —c1992, 2nd ed.)
- Ramella, M., Geller, M. J., & Huchra, J. P. 1989, *ApJ*, 344, 57
- Sandage, A. & Visvanathan, N. 1978, *ApJ*, 225, 742
- Smail, I., Kuntschner, H., Kodama, T., Smith, G. P., Packham, C., Fruchter, A. S., & Hook, R. N. 2001, *MNRAS*, 323, 839
- Smail, I., Morrison, G., Gray, M. E., Owen, F. ., Ivison, R. J., Kneib, J.-P., & Ellis, R. S. 1999, *ApJ*, 525, 609
- Stanford, S. A., Eisenhardt, P. R., & Dickinson, M. 1998, *ApJ*, 492, 461
- Terlevich, A. I., Caldwell, N., & Bower, R. G. 2001, *MNRAS*, 326, 1547
- Terlevich, A. I., Kuntschner, H., Bower, R. G., Caldwell, N., & Sharples, R. M. 1999, *MNRAS*, 310, 445
- Thomas, D., Maraston, C., Bender, R., & de Oliveira, C. M. 2005, *ApJ*, 621, 673
- Trager, S. C., Faber, S. M., Worthey, G., & González, J. J. 2000, *AJ*, 120, 165
- Tran, K. H., Franx, M., Illingworth, G., Kelson, D. D., & van Dokkum, P. 2003a, *ApJ*, 599, 865
- Tran, K. H., Franx, M., Illingworth, G. D., van Dokkum, P., Kelson, D. D., & Magee, D. 2004, *ApJ*, 609, 683
- Tran, K. H., Kelson, D. D., van Dokkum, P., Franx, M., Illingworth, G. D., & Magee, D. 1999, *ApJ*, 522
- Tran, K. H., Simard, L., Illingworth, G., & Franx, M. 2003b, *ApJ*, 590, 238
- Tran, K. H., van Dokkum, P., Illingworth, G. D., Kelson, D., Gonzalez, A., & Franx, M. 2005a, *ApJ*, 619, 134
- Tran, K.-V. H., van Dokkum, P., Franx, M., Illingworth, G. D., Kelson, D. D., & Schreiber, N. M. F. 2005b, *ApJ*, 627, L25
- Valdes, F. 1982, *Faint Object Classification and Analysis System Manual*
- van Dokkum, P. G., Franx, M., Fabricant, D., Illingworth, G. D., & Kelson, D. D. 2000, *ApJ*, 541, 95
- van Dokkum, P. G., Franx, M., Fabricant, D., Kelson, D. D., & Illingworth, G. D. 1999, *ApJ*, 520, L95
- van Dokkum, P. G., Franx, M., Kelson, D. D., Illingworth, G. D., Fisher, D., & Fabricant, D. 1998, *ApJ*, 500, 714+
- Worthey, G. & Ottaviani, D. L. 1997, *ApJS*, 111, 377
- Wuyts, S., van Dokkum, P. G., Kelson, D. D., Franx, M., & Illingworth, G. D. 2004, *ApJ*, 605, 677
- Yee, H. K. C., Ellingson, E., & Carlberg, R. G. 1996, *ApJS*, 102, 269+

TABLE 1
MS 1054-03 MEMBERS

HST#	z	Q_z^a	B# ^b	i_{775}^b	$(V - i_{775})^b$	T-type ^c	$\Delta(\text{RA})^d$	$\Delta(\text{Dec})^d$	OII ^e	\pm	H δ^e	\pm	H γ^e	\pm	σ_{1D}^f
Absorption															
H1192	0.8390	3	B5324	20.77	1.675	0(99)	136.6	-57.9	-0.2	0.7	0.2	0.6	1.5	0.7	137 [†]
H1464	0.8391	3	B8438	21.46	1.604	-2	130.9	-25.2	-1.3	1.6	2.0	1.2	-2.4	1.4	174
H1609	0.8296	3	B8222	21.89	1.643	-4	120.1	2.6	3.3	1.9	-4.2	1.7	-2.0	1.8	188
H1649	0.8373	3	B8456	21.11	1.650	-4	122.6	-16.4	0.4	1.4	1.0	0.9	3.1	1.0	243 [†]
H2169	0.8324	3	B4353	21.69	1.653	-2	91.0	-63.4	4.9	1.6	4.2	1.2	3.7	1.5	170
H2409	0.8372	3	B3718	21.76	1.736	-4	84.4	-23.7	0.5	1.5	1.7	1.2	-3.8	1.3	287 [†]
H2525	0.8323	3	B4254	23.44	1.591	-5	75.8	-38.5	-0.5	2.8	-6.8	2.7	3.0	3.2	71
H2812	0.8274	3	B4137	22.95	1.538	-4	68.3	-24.2	0.8	2.9	1.9	2.7	-1.7	3.5	102
H2881	0.8374	3	B8362	22.20	1.511	-1	68.3	56.0	3.0	2.7	4.8	1.7	3.1	1.8	156
H2977	0.8316	3	B4778	22.77	1.518	-2	61.5	-49.4	2.3	2.1	-4.9	2.1	5.7	2.4	110
H3058	0.8309	3	B4167	20.31	1.593	-5	52.8	-9.5	1.8	1.1	1.7	0.9	0.5	1.0	303 [†]
H3105	0.8275	3	B4324	21.84	1.539	-5	64.8	-29.3	0.7	1.0	3.9	0.9	1.0	1.1	142
H3212	0.8392	3	B2175	22.23	1.611	-1(99)	54.5	-132.2	0.9	2.3	-2.9	2.0	-3.6	2.4	155
H3288	0.8324	3	B4363	23.58	1.680	-5	49.6	-12.1	7.1	3.6	2.0	3.0	-4.8	3.8	125
H3398	0.8343	3	B4212	23.18	1.607	-5	47.7	-2.5	-3.9	4.5	-4.4	3.8	0.4	4.2	116
H3495	0.8199	3	B4213	22.07	1.613	-2(99)	46.1	-1.5	1.2	2.2	3.6	2.5	2.8	3.1	190
H3524	0.8195	3	B4214	22.08	1.522	-1(99)	44.9	-1.3	1.8	2.0	6.6	2.3	-6.1	3.1	148
H3532	0.8302	3	B2787	22.77	1.634	-4	42.9	-76.5	-2.9	3.2	0.9	2.7	-11.6	4.0	110
H3581	0.8352	3	B4358	21.68	1.603	-5	43.8	-5.4	2.0	1.7	2.6	1.3	1.6	1.5	193
H3596	0.8173	3	B4942	21.82	1.520	-4	41.3	-34.2	0.6	0.4	1.7	0.5	1.5	0.8	125
H3768	0.8177	3	B4364	21.38	1.612	-5	38.9	-0.2	-2.5	1.4	1.9	1.2	1.3	1.5	221 [†]
H3816	0.8238	3	B2874	22.15	1.644	-2	33.5	-56.8	1.2	1.6	4.1	1.4	2.6	1.9	179
H3835	0.8396	3	B8262	21.46	1.586	-5	39.7	96.5	2.2	1.3	3.0	1.1	3.7	1.2	169
H3995	0.8339	3	B2390	21.23	1.633	-5	30.9	-80.9	-0.9	1.3	1.4	1.1	-0.6	1.3	229
H4012	0.8309	3	B2391	21.82	1.592	-5	31.4	-82.7	-2.7	1.3	4.1	0.9	-1.5	1.2	133
H4031	0.8218	3	B3185	22.14	1.621	-5	26.1	-31.1	4.1	1.7	-4.9	2.0	-0.5	2.3	161
H4039	0.8416	3	B5134	23.22	1.211	-4	22.8	-22.1	0.3	3.3	1.8	2.9	0.8	3.3	67
H4222	0.8443	3	B4620	21.42	0.970	6	22.9	5.9	2.0	2.2	-9.0	2.4	-2.5	2.9	...
H4343	0.8378	3	B7835	22.13	1.600	-2	18.3	161.2	1.0	2.5	-0.6	1.7	2.6	1.9	119
H4345	0.8349	3	B5006	21.01	1.674	-5	21.6	-13.1	0.9	0.9	-1.3	0.8	2.2	0.8	335 [†]
H4428	0.8253	3	B5062	22.18	1.579	-2	12.1	-5.5	3.9	1.6	0.4	1.8	4.6	2.0	135
H4459/4528	0.8260	3	B4169	22.93	1.544	-5(99)	10.3	44.6	-0.1	2.1	2.3	2.0	-0.3	2.2	93
H4459	0.8265	3	B4169	22.93	1.544	-5(99)	10.3	44.6	1.7	1.2	2.3	1.3	1.0	1.6	93
H4520	0.8316	3	B2830	19.87	1.705	-5	0.0	0.0	0.2	1.0	0.7	0.7	1.0	0.7	322 [†]
H4715	0.8339	3	B5099	22.49	1.639	-2	2.1	4.3	0.3	3.1	5.2	2.7	-2.1	2.7	172
H4822	0.8333	3	B3148	22.43	1.494	10	-0.4	3.2	5.0	3.2	-2.6	2.7	3.7	2.8	50
H4870	0.8308	3	B2589	21.81	1.544	-5	-3.6	-31.3	1.8	1.7	1.9	1.5	1.6	1.8	281 [†]
H4922	0.8280	3	B5116	22.32	1.644	-4	-5.7	12.5	-1.0	2.2	-1.6	2.0	3.9	2.2	168
H4926	0.8252	3	B3035	21.77	1.719	-3	-4.2	-3.7	1.0	1.6	0.8	1.4	-0.6	1.6	310 [†]

TABLE 1—*Continued*

HST#	z	Q_z^a	B# ^b	i_{775}^b	$(V - i_{775})^b$	T-type ^c	$\Delta(\text{RA})^d$	$\Delta(\text{Dec})^d$	OII ^e	\pm	H δ^e	\pm	H γ^e	\pm	σ_{1D}^f
H5111	0.8186	3	B2301	22.20	1.558	-5	-13.8	-37.4	2.0	1.7	3.5	1.6	1.7	2.0	131
H5280	0.8301	3	B3070	21.63	1.649	-2	-21.6	20.6	1.0	1.9	-1.1	1.5	3.4	1.8	259 [†]
H5196	0.8418	3	B2741	21.39	1.645	-2	-16.6	0.2	2.4	1.5	5.8	1.2	0.5	1.5	301 [†]
H5216	0.8351	3	B2403	21.31	1.555	1	-24.1	-5.6	-3.3	3.2	3.9	1.7	3.4	2.0	152
H5226	0.8348	3	B5072	22.17	1.618	-2	-18.8	31.1	-2.5	2.9	1.9	1.7	0.5	2.2	204
H5269	0.8243	3	B2901	22.28	1.551	-5	-21.7	9.3	3.0	1.6	-3.3	1.7	-0.6	2.0	163
H5298	0.8311	3	B3031	21.95	1.593	-2	-21.9	19.3	1.3	2.1	1.2	1.7	0.9	2.1	283 [†]
H5325	0.8314	3	B1509	22.37	1.592	-5	-24.5	-79.5	-0.9	4.2	0.4	2.8	-6.8	3.5	102
H5338	0.8293	3	B3131	22.58	1.630	-4	-24.3	23.7	-1.5	2.0	2.2	1.7	2.1	2.0	113
H5347	0.8251	3	B4987	21.02	1.544	-1(99)	-34.6	56.3	0.5	1.9	3.1	1.8	3.3	2.3	253 [†]
H5432	0.8149	3	B2651	22.39	1.252	-1	-29.6	2.3	-1.8	0.8	10.4	0.6	-8.8	1.0	62
H5442	0.8201	3	B2639	22.35	1.549	-5	-29.9	4.5	-0.4	2.5	0.1	2.3	5.2	2.7	121
H5450	0.8365	3	B2143	20.58	1.612	-5	-46.4	-3.6	-1.0	2.0	1.0	1.1	0.1	1.2	233 [†]
H5529	0.8218	3	B2894	21.56	1.643	-5	-38.0	31.2	-2.2	1.3	2.4	1.1	2.5	1.4	182 [†]
H5541	0.8276	3	B3241	22.57	1.610	-1	-36.1	45.8	-4.2	3.2	2.1	2.6	4.8	2.6	132
H5543	0.8246	3	B4988	21.96	1.604	-5	-35.4	55.5	-0.4	3.0	2.7	2.8	-1.5	3.5	220
H5577	0.8310	3	B3052	21.54	1.597	-4	-43.8	48.1	2.5	1.4	0.0	1.1	4.5	1.3	305 [†]
H5607	0.8294	3	B3113	22.19	1.649	-5	-42.1	46.0	4.4	4.5	5.3	4.0	-3.3	5.2	138
H5666	0.8315	3	B830	20.82	1.641	-1	-57.8	-83.9	2.0	1.2	1.3	0.9	0.4	1.0	285 [†]
H5672	0.8306	3	B2709	21.88	1.597	-5	-46.8	30.2	0.6	3.8	8.4	2.3	-10.6	3.8	180
H5720	0.8240	3	B4374	22.01	1.538	-4	-44.0	100.9	-1.4	1.6	5.3	1.4	-1.3	1.8	178
H5756	0.8305	3	B4766	21.22	1.628	-5	-59.7	97.7	-2.4	1.2	1.4	0.9	-1.7	1.0	231 [†]
H5757	0.8207	3	B2257	21.65	1.616	-5	-49.6	1.3	-3.3	1.6	-0.2	1.3	1.9	1.5	167
H6036/6064	0.8333	3	B1496	21.41	1.619	-5(99)	-63.5	-29.3	-0.3	1.4	3.4	0.9	1.3	1.0	253 [†]
H6038	0.8312	3	B2353	21.17	1.641	-5	-61.7	28.1	-0.2	0.4	1.2	0.3	-0.2	0.4	253
H6048	0.8304	3	B2041	23.25	1.463	-5	-63.1	-0.5	1.3	4.0	0.5	3.1	-0.3	3.8	136
H6064	0.8341	3	B1461	21.56	1.541	-5(99)	-63.6	-29.8	1.7	0.9	3.4	0.8	0.6	0.8	181
H6301	0.8277	3	-70.8	25.2	1.6	1.3	3.4	1.1	0.2	1.2	248 [†]
H6412	0.8322	3	B2385	22.75	1.702	-1	-70.8	35.5	2.1	3.9	4.4	3.0	-2.0	4.0	102
H6516	0.8289	3	B1644	22.98	0.913	-2	-75.8	-9.4	0.3	3.0	0.2	3.3	-2.9	4.1	37
H6567	0.8265	3	B654	21.46	1.614	1(99)	-89.2	-59.9	-4.6	3.2	4.3	2.0	2.4	2.4	201 [†]
H6645	0.8213	3	B1111	22.23	1.166	-2	-85.1	-34.0	-3.4	1.8	6.4	2.0	1.3	2.8	64
H7079	0.8351	3	B984	21.86	1.564	-5	-118.8	-0.8	0.1	0.8	3.0	0.6	1.7	0.8	132
H7746	0.8252	3	B2315	21.68	1.702	-2	-134.2	111.0	0.3	1.3	-1.4	1.2	-1.5	1.3	268
Post-starburst															
H2710	0.8420	3	B3224	21.85	1.588	-4	75.8	-88.8	-2.7	2.3	3.3	1.7	7.1	2.0	140
H2872	0.8340	3	B4488	21.58	1.454	0	67.6	-40.7	-1.3	1.4	6.1	1.1	3.2	1.4	179 [†]
H3910	0.8332	3	B4735	21.41	1.975	-2	32.1	-11.7	-0.5	1.3	2.6	1.0	6.2	1.3	295 [†]
H4389	0.8292	3	B4366	21.78	1.131	8(99)	14.3	29.8	-3.9	3.1	8.5	2.2	5.9	2.9	...
H4390	0.8240	3	B4305	22.55	1.573	-5	13.3	34.1	2.8	2.5	4.6	2.2	6.0	2.8	...

TABLE 1—*Continued*

HST#	z	Q_z^a	B# ^b	i_{775}^b	$(V - i_{775})^b$	T-type ^c	$\Delta(\text{RA})^d$	$\Delta(\text{Dec})^d$	OII ^e	\pm	H δ^e	\pm	H γ^e	\pm	σ_{1D}^f
H5359	0.8238	3	B2649	20.63	1.460	1	-26.4	6.9	0.4	1.0	5.6	0.8	6.0	1.0	138 [†]
H5534	0.8395	3	B2937	21.33	1.519	-4	-38.2	34.1	-1.4	1.3	5.6	1.0	3.4	1.2	152
H5691	0.8331	3	B2476	22.64	1.643	-1	-44.3	11.5	-0.5	3.2	3.0	2.4	8.5	2.2	152
H5786	0.8344	3	B2178	22.38	1.604	-2	-51.0	-4.4	10.9	3.8	1.6	2.3	9.7	2.5	140
H5833	0.8262	3	B1859	22.24	1.530	1	-54.9	-19.0	0.5	1.3	0.3	1.3	7.8	1.7	86
H5840	0.8259	3	B2468	21.05	1.487	-1(99)	-52.4	22.9	-1.3	0.6	7.4	0.5	7.7	0.6	211 [†]
H5923	0.8392	3	B3180	21.25	1.513	3	-57.8	73.2	-3.7	1.4	8.1	0.9	6.6	1.2	165
H5926	0.8231	3	B2333	22.40	1.386	-1	-55.2	16.6	-2.4	2.8	11.8	2.2	10.0	3.0	68
H6164	0.8257	3	B2328	22.01	1.643	-5	-63.5	28.1	0.2	5.1	4.2	4.4	4.5	5.4	174
H6309	0.8284	3	B1772	22.77	1.430	-4	-67.3	-10.0	1.4	2.9	6.5	2.6	5.4	3.5	56
H8001	0.8444	3	B2226	25.52	1.144	9	-111.9	69.5	-2.7	2.1	10.3	1.3	9.6	1.7	165
H987	0.8251	3	B6304	21.74	1.712	-2	152.4	81.4	-2.4	1.1	4.7	0.9	4.1	1.1	221
Emission															
H1242	0.8286	3	B3386	22.67	0.830	4	137.3	-70.9	-40.6	3.3	8.3	1.9	-14.4	3.0	29
H1532	0.8219	3	B6995	21.82	0.875	6(99)	128.9	86.4	-9.4	3.6	1.0	3.0	11.6	4.2	35
H159	0.8228	3	B6011	22.57	0.857	6	208.7	50.1	-24.4	2.3	5.5	2.0	-3.5	2.9	21
H2334	0.8453	3	B4015	22.33	1.473	-1	82.3	-35.4	-5.9	2.6	4.6	1.5	1.2	1.9	120
H2377	0.8369	3	B8422	21.86	1.359	1	85.1	31.5	-6.9	2.2	6.5	1.5	6.6	2.0	79
H2538	0.8179	3	B3739	23.16	1.493	-5	75.3	-12.8	-12.0	3.3	-1.0	2.1	-14.1	3.0	106
H255	0.8346	3	B6736	22.22	1.041	3	187.8	35.0	-23.1	5.8	4.1	3.2	2.2	5.8	24
H2609	0.8362	3	B3686	22.67	1.587	-4	75.2	-11.0	-5.6	4.5	3.8	2.6	6.5	3.4	...
H3043	0.8278	3	B4308	23.48	1.403	-4	59.9	-22.5	-6.6	4.3	4.4	3.4	11.3	4.5	64
H3284	0.8449	3	B2503	21.41	1.005	4	53.9	-93.9	-5.3	1.7	3.9	1.5	-1.8	1.9	48
H3585	0.8366	3	B3795	23.83	1.426	-1	39.8	27.1	-16.1	9.6	7.1	5.9	-11.7	8.3	37
H4223	0.8303	3	B2844	22.48	0.905	-1(99)	18.4	-41.1	-5.1	2.6	7.5	2.1	2.5	2.8	34
H4683/4741	0.8329	3	B3812	21.65	0.274	8(99)	6.9	65.5	-56.8	1.5	-1.2	0.9	-6.2	1.2	...
H4683	0.8332	3	B3812	21.65	0.274	8(99)	6.9	65.5	-60.7	2.4	-3.8	1.5	...	0.0	...
H4705	0.8453	3	B4954	21.22	1.289	1	6.0	8.4	-5.6	1.2	6.1	0.9	5.7	1.0	253 [†]
H5599	0.8112	3	B1978	21.95	0.924	4	-57.0	-5.6	-13.7	2.4	2.4	1.6	0.7	2.1	...
H5955	0.8293	3	B1814	22.65	1.423	-5	-60.5	-14.0	-5.3	4.3	5.3	3.2	12.9	4.4	...
H5992	0.8306	3	B1679	22.44	1.125	1	-58.1	-25.2	-5.3	3.1	0.5	2.5	-6.5	4.0	39
H6372	0.8332	3	B754	22.79	1.324	3	-75.5	-73.5	-8.0	6.4	6.3	2.7	7.9	3.4	42
H6695	0.8352	3	B845	22.50	1.743	-2	-90.2	-44.3	-7.1	3.7	-1.8	2.2	-48.1	3.3	150
H6812	0.8397	3	B2218	22.76	0.922	3	-97.9	56.7	-21.0	3.8	3.1	3.6	2.3	4.6	...
H7107	0.8412	3	B2991	22.45	0.719	1	-106.2	116.8	-40.4	3.3	-4.2	2.7	10.3	2.8	...
H7163	0.8255	3	B156	23.54	0.843	0	-186.0	12.4	-34.7	8.0	8.6	5.5	5.1	6.6	17
H7186	0.8246	3	B24	22.80	0.811	-1	-203.5	24.1	-26.3	3.3	5.1	2.7	8.4	4.0	18
H7333	0.8446	3	B2926	24.04	0.254	8	-119.9	127.8	-42.7	10.0	18.2	11.9	9
H7335	0.8280	3	B215	22.16	0.806	4	-174.8	5.6	-33.5	5.3	10.5	3.8	2.5	5.9	32
No Measured [OII]															

TABLE 1—*Continued*

HST#	z	Q_z^a	B# ^b	i_{775}^b	$(V - i_{775})^b$	T-type ^c	$\Delta(\text{RA})^d$	$\Delta(\text{Dec})^d$	OII ^e	\pm	H δ^e	\pm	H γ^e	\pm	σ_{1D}^f
H1942	0.8310	3	B3652	22.01	1.578	-1	99.2	-38.5	-1.1	1.0	164
H2203	0.8314	3	B4049	22.80	1.574	-2	85.9	-41.0	0.4	2.4	-4.0	3.1	116
H6688	0.8353	3	B846	21.32	1.628	-5	-91.6	-42.0	1.3	1.0	1.7	1.2	274 [†]
H6690	0.8241	3	B3003	22.50	1.366	4	-85.4	91.7	-0.5	1.8	2.5	2.3	...
H7228	0.8049	3	B308	23.77	1.425	-5	-108.9	-70.0	4.4	9.4	1.8	9.1	65
Probable Members															
H7901	0.8310	2	B311	22.93	0.686	3	-175.7	11.3	-4.4	2.8	3.4	2.9	12.9	4.0	...
H7210	0.8270	2	B732	23.24	0.880	3	-184.4	54.6	-31.3	9.6	14.6	6.4	6.7	8.4	...
H7076	0.8456	2	B2225	23.44	0.626	-1	-104.5	65.7	-0.8	7.1	24.6	8.9	10.4	12.1	...
H6829	0.8294	2	B2898	23.05	0.740	1	-91.2	92.0	-43.2	6.6	1.2	4.9	5.1	5.5	...
H6065	0.8253	2	B3692	22.21	1.167	6	-58.2	150.4	-11.2	3.5	5.9	2.9	0.4	3.4	...
H5922	0.8318	2	B4717	23.40	1.358	8	-60.2	102.5	-7.3	4.6	8.0	4.0	-1.1	7.4	...
H5555	0.8209	2	B2577	22.45	1.551	-4	-38.0	8.1	0.6	2.2	4.0	2.3	-4.2	2.8	...
H4165	0.8315	2	B5048	23.61	1.153	-4	18.2	-11.2	5.2	4.7	5.9	4.9	17.1	6.4	...
H3447	0.8381	2	B2873	23.12	1.445	3	45.6	-74.7	-3.8	3.6	-5.6	2.7	-11.5	2.9	...
H3356	0.8358	2	B2896	22.97	1.446	-4	49.0	-79.0	3.6	3.3	1.7	3.0	10.0	3.8	...
H2746	0.8307	2	B4063	23.09	1.468	-2	70.0	-22.9	1.2	10.6	24.6	10.2	-6.2	14.6	...
H2467	0.8433	2	B5472	23.37	1.620	-4	77.7	24.1	5.0	5.9	12.9	4.2	-2.4	6.5	...
H1724	0.8374	2	B8312	22.72	1.635	-1	111.0	9.4	-11.4	7.4	7.1	4.3	5.7	5.1	...
H925	0.8245	2	B5532	22.88	1.662	-1	151.9	-62.0	-1.9	2.5	-6.5	2.2	9.6	2.3	...
H426	0.8263	2	B7431	22.78	1.279	-1	186.6	-14.5	-4.7	4.3	6.3	4.1	8.6	5.5	...
H7603	0.8288	1	B1192	23.55	0.708	3	-140.6	39.4	-57.5	19.1	5.7	11.0
H7212	0.8283	1	B632	23.10	0.662	4	-180.3	47.3	-40.7	5.2	8.5	3.7	-1.5	5.6	...
H6993	0.8291	1	B2484	23.74	0.688	3	-100.5	78.1	14.3	11.5	19.1	9.1	...
H6663	0.8372	1	B2240	23.67	0.789	0	-84.4	41.5	-32.0	9.0	-15.3	12.8	9.8	13.2	...
H5990	0.8334	1	B5082	22.70	0.442	8	-67.5	89.5	-8.6	3.3	-1.0	4.7	0.3	5.9	...
H5935	0.8369	1	B2547	22.60	1.026	3	-53.6	27.5	-0.7	2.9	5.9	2.7	2.3	3.2	...
H5545	0.8229	1	B2356	23.66	0.499	8	-36.6	-5.9	45.8	14.9	...
H4028	0.8286	1	B5447	22.46	0.847	3	29.6	83.3	-80.7	23.9	-5.4	8.9	-13.9	8.4	...
H1266	0.8264	1	B8107	23.37	0.665	-1	135.8	-3.2	-32.2	5.4	-4.8	4.2	-0.6	4.3	...

^aIn our analysis, we consider only members with a redshift quality flag of 3. The typical redshift errors from the cross-correlation are $\sim 30 \text{ km s}^{-1}$, and we find that the median error estimated from galaxies observed in multiple masks is 50 km s^{-1} . Candidate members with $Q_z = 2$ or 1 are listed at the end of the table.

^bThe identification number and corresponding ACS photometry for the cluster galaxies are from Blakeslee et al. (2006); magnitudes and colors (AB system) are measured within an effective radius determined from fitting 2-D Sérsic profiles. At $z = 0.83$, i_{775} and $(V - i_{775})$ closely correspond to rest-frame B and $(U - B)$.

^cThe morphological types as assigned by Postman et al. (2005) using the ACS imaging; members that are also visually classified to be part of a merging system (van Dokkum et al. 2000) have “(99)”.

^dThe relative offset in arcseconds determined with respect to the brightest cluster galaxy (H4520); the BCG’s J2000 coordinates are $(10^h 57^m 00^s .0, -3^\circ 37' 36'' .2)$. Positive $\Delta(\text{RA})$ is west and positive $\Delta(\text{Dec})$ is north.

^eEquivalent widths and their errors are in Å; the indices are determined using the same bandpasses as Fisher et al. (1998).

^fThe 27 members where the internal velocity dispersion (km s^{-1}) is measured directly (Wuyts et al. 2004) are daggered and have errors of $\pm 10 \text{ km s}^{-1}$. The 11 members where the internal velocity dispersion is estimated from the observed velocity distribution (Wuyts et al. 2004) are not daggered and have errors of $\pm 10 \text{ km s}^{-1}$.

TABLE 2
OBSERVED ($V - i_{775}$): MEAN COLOR OFFSET AND SCATTER

Galaxy Type ^a	N_g	Offset ^b	σ_{obs} ^b	σ_{int} ^c	$\langle V - i_{775} \rangle^b$	$\langle i_{775} - z \rangle^b$
Absorption	72	0.001 ± 0.007	0.056 ± 0.006	0.048 ± 0.009	1.605 ± 0.007	0.675 ± 0.008
Absorption: Red, Bright ^d	37	0.000 ± 0.008	0.050 ± 0.007	0.047 ± 0.008	1.616 ± 0.009	0.694 ± 0.013
Absorption: Red, Faint ^d	30	-0.003 ± 0.012	0.060 ± 0.008	0.055 ± 0.009	1.587 ± 0.013	0.664 ± 0.010
E+A	17	-0.082 ± 0.040	0.168 ± 0.050	0.152 ± 0.052	1.528 ± 0.038	0.531 ± 0.045
Emission	26	-0.535 ± 0.103	0.417 ± 0.063	0.407 ± 0.064	1.054 ± 0.104	0.351 ± 0.048
E+S0	94	-0.009 ± 0.009	0.078 ± 0.009	0.072 ± 0.010	1.595 ± 0.009	0.673 ± 0.009
Elliptical Only	55	-0.011 ± 0.009	0.063 ± 0.008	0.055 ± 0.008	1.592 ± 0.011	0.675 ± 0.009
Elliptical: Red, Bright ^d	29	-0.008 ± 0.012	0.049 ± 0.010	0.045 ± 0.011	1.607 ± 0.011	0.697 ± 0.016
Elliptical: Red, Faint ^d	25	-0.025 ± 0.019	0.077 ± 0.011	0.071 ± 0.013	1.560 ± 0.026	0.651 ± 0.013
S0 Only	39	-0.005 ± 0.022	0.112 ± 0.030	0.102 ± 0.032	1.595 ± 0.025	0.659 ± 0.049
S0: Red, Bright ^d	13	0.016 ± 0.030	0.091 ± 0.042	0.085 ± 0.042	1.623 ± 0.037	0.700 ± 0.032
S0: Red, Faint ^d	19	-0.002 ± 0.024	0.075 ± 0.017	0.068 ± 0.018	1.596 ± 0.024	0.671 ± 0.028
Spiral+Irr	26	-0.501 ± 0.089	0.395 ± 0.064	0.273 ± 0.065	1.096 ± 0.085	0.364 ± 0.036

^aSpectral types were assigned using [OII] λ 3727, H δ , and H γ (see §2.4.3). Morphological types were classified using HST/ACS imaging (see §2.2; Postman et al. 2005).

^bThe mean offset and observed scatter in ($V - i_{775}$) as well as the mean colors were determined using the biweight estimator (Beers et al. 1990).

^cFollowing B06, we correct the observed scatter in color for measurement errors.

^dGalaxies are red if $\Delta(V - i_{775}) \geq -0.2$. We divide the members into bright and faint samples using $i_{775} = 22$ (note that $i_{775}^* = 22.3$; Goto et al. 2005).

TABLE 3
REDSHIFTED ($U - V$)_z: MEAN COLOR OFFSET AND SCATTER^a

Galaxy Type ^b	N_g	Offset ^c	σ_{obs} ^c	σ_{int} ^d
Absorption	72	0.000 ± 0.011	0.091 ± 0.009	0.083 ± 0.012
E+A	17	-0.192 ± 0.084	0.282 ± 0.041	0.266 ± 0.044
Emission	26	-0.779 ± 0.129	0.564 ± 0.076	0.554 ± 0.077
E+S0	94	0.005 ± 0.012	0.116 ± 0.019	0.110 ± 0.020
Elliptical Only	55	-0.006 ± 0.015	0.095 ± 0.013	0.087 ± 0.015
S0 Only	39	0.010 ± 0.043	0.197 ± 0.062	0.187 ± 0.063
Spiral+Irregular	26	-0.742 ± 0.109	0.497 ± 0.072	0.485 ± 0.073

^aThe CM relation was determined using the same 67 red absorption-line members as the CM relation used in Table 2.

^bSpectral types were assigned using [OII] λ 3727, H δ , and H γ (see §2.4.3). Morphological types were classified using HST/ACS imaging (see §2.2; Postman et al. 2005).

^cThe mean offset and observed scatter in ($U - V$)_z as well as the mean colors were determined using the biweight estimator (Beers et al. 1990).

^dFollowing B06, we correct the observed scatter in color for measurement errors.

TABLE 4
INDICES OF COMPOSITE SPECTRA

Galaxy Type	N_g ^a	[OII] ^{bc}	H δ ^{bc}	H γ ^{bc}	H δ_A ^{cd}	$D_N(4000)$ ^{cd}
Absorption	71	0.7 \pm 0.0	1.7 \pm 0.0	0.2 \pm 0.1	0.5 \pm 0.0	1.67 \pm 0.00
Abs, $0.0 \leq \Delta(V - i_{775}) \leq 0.1$	36	0.2 \pm 0.1	1.3 \pm 0.1	0.3 \pm 0.1	0.1 \pm 0.1	1.73 \pm 0.00
Abs, $-0.1 \leq \Delta(V - i_{775}) < 0.0$	25	1.0 \pm 0.1	2.1 \pm 0.1	1.2 \pm 0.1	1.0 \pm 0.1	1.66 \pm 0.01
E+A	17	-0.4 \pm 0.2	5.7 \pm 0.2	5.9 \pm 0.1	4.4 \pm 0.2	1.55 \pm 0.01
Emission	26	-24.6 \pm 0.6	3.8 \pm 0.1	-4.4 \pm 0.8	4.2 \pm 0.2	1.24 \pm 0.01
E+S0	90	-0.9 \pm 0.1	2.5 \pm 0.0	0.8 \pm 0.1	1.4 \pm 0.0	1.62 \pm 0.00
Elliptical	53	-0.1 \pm 0.1	1.9 \pm 0.1	0.8 \pm 0.1	0.7 \pm 0.1	1.66 \pm 0.00
Elliptical: Red, Bright ^e	28	-0.0 \pm 0.1	2.2 \pm 0.1	0.7 \pm 0.1	1.3 \pm 0.1	1.70 \pm 0.01
S0	37	-2.2 \pm 0.3	3.3 \pm 0.1	0.5 \pm 0.2	2.5 \pm 0.1	1.58 \pm 0.01
S0: Red, Bright ^e	12	0.4 \pm 0.1	3.1 \pm 0.2	2.4 \pm 0.2	2.5 \pm 0.2	1.67 \pm 0.02
Sp+Irr	25	-23.1 \pm 1.1	3.6 \pm 0.2	-1.8 \pm 1.1	3.8 \pm 0.2	1.27 \pm 0.01
Red Mergers ^f	17	0.9 \pm 0.1	2.5 \pm 0.2	0.4 \pm 0.6	0.5 \pm 0.2	1.70 \pm 0.01
Field E+A ^g	6	-1.5 \pm 0.4	4.6 \pm 0.2	4.9 \pm 0.3	4.3 \pm 0.2	1.36 \pm 0.02

^aThe number of individual spectra combined to determine the composite spectrum; the five cluster galaxies that do not have measured [OII] λ 3727 are excluded.

^bWe use the same bandpasses defined in Fisher et al. (1998) to measure these spectral indices; the equivalent widths are in Å. The continuum sidebands are further way from the line center than those used for measuring, *e.g.* H δ_A , to accommodate the wider wings of strong Balmer absorption.

^cThe errors were determined by generating 1000 composite spectra from the base set for each galaxy type by bootstrap, measuring the same spectral line, taking the biweight scale of the distribution (Beers et al. 1990), and dividing that scale by $\sqrt{N_g}$.

^dTo compare to the star formation histories in Kauffmann et al. (2003), we use their defined bandpasses to measure H δ_A (Å) and $D_N(4000)$.

^eAs in Table 2, members are bright and red if $i_{775} < 22$ and $\Delta(V - i_{775}) \geq -0.2$.

^fComposite spectrum of the 17 members that are spectroscopically confirmed to be in red, merging systems by Tran et al. (2005a)

^gComposite field E+A spectrum ($0.3 < z < 1$; $\bar{z} = 0.6$) from Tran et al. (2004).

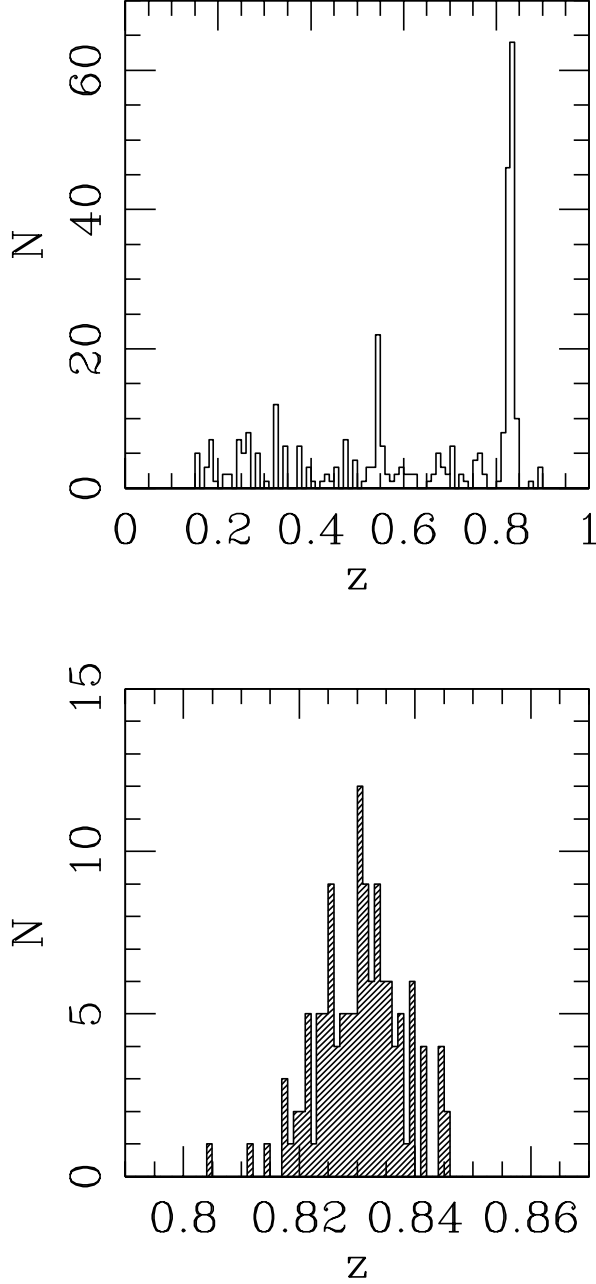


FIG. 1.— From our catalog of 433 redshifts in the MS1054 field, we show the redshift distribution of the 307 galaxies at $0 < z < 1$ with quality flags of 3 (top), and an expanded view of the 129 galaxies ($Q_z = 3$) that are in MS1054 (bottom). Using these 129 members, MS1054’s mean redshift and velocity dispersion are $z = 0.8307 \pm 0.0004$ and $\sigma_z = 1156 \pm 82 \text{ km s}^{-1}$, respectively.

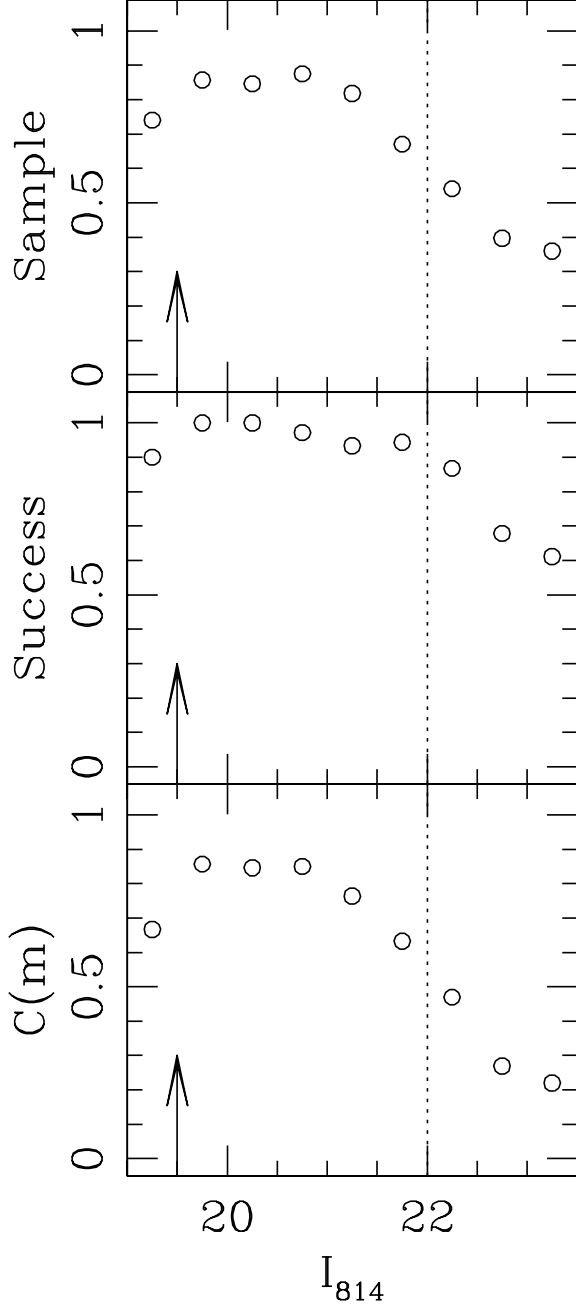


FIG. 2.— *Top*: The sampling rate, defined as the number of spectroscopic targets divided by the number of galaxies in the photometric catalog, is shown as a function of magnitude (bin size ± 0.5 mags); we consider only objects on the WFPC2 mosaic. The BCG's magnitude ($I_{814} = 19.5$) is indicated by the arrow. *Middle*: The number of acquired redshifts divided by the number of targets: at $I_{814} = 22$ (dotted line), the success rate remains $\sim 90\%$. *Bottom*: The completeness, defined as the number of redshifts divided by the number of galaxies in the photometric catalog: incompleteness at the faint end is due to sparse sampling and not the inability to measure redshifts of targeted galaxies.

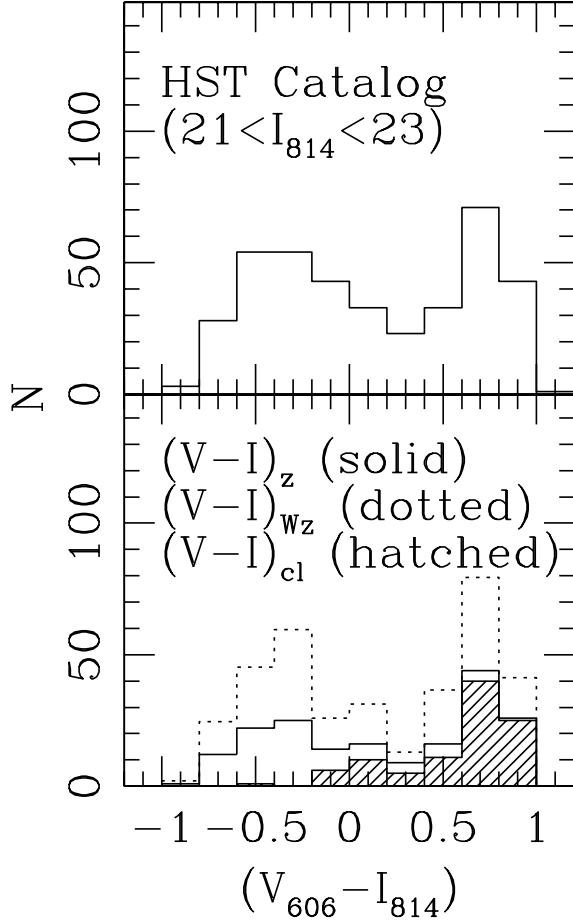


FIG. 3.— The color distribution $(V_{606} - I_{814})$ of all galaxies in the WFPC2 catalog with $21 < I_{814} < 23$; the bin size is 0.2. *Bottom:* The $(V_{606} - I_{814})_z$ distribution for all galaxies on the WFPC2 mosaic with redshifts (solid line) as well as cluster members on the mosaic (hatched) in the same magnitude range. We include the weighted color distribution $(V_{606} - I_{814})_{Wz}$ (dotted) of the redshift sample where each galaxy is weighted by the inverse of the magnitude selection function $C(m)$. A K-S test finds $(V_{606} - I_{814})_{Wz}$ is indistinguishable from $(V_{606} - I_{814})$, *i.e.* there is no measurable bias against faint red (passive) galaxies in the spectroscopic sample after correcting for sparse sampling.

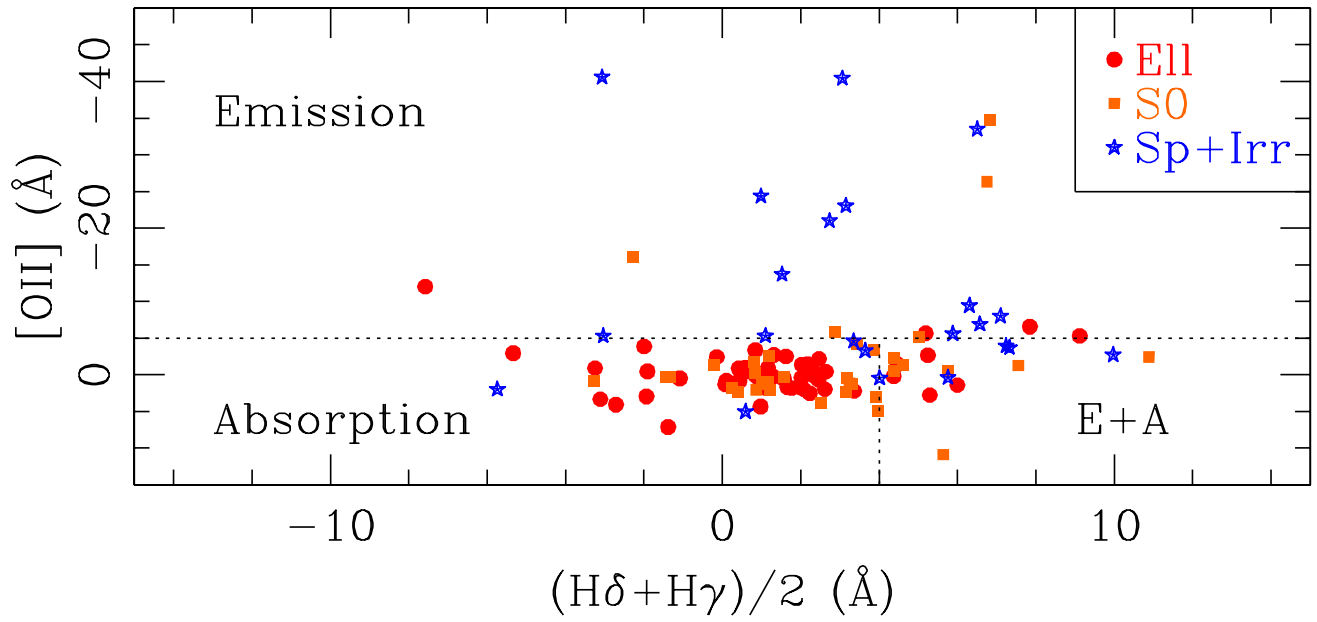


FIG. 4.— The distribution of [OII]λ3727 versus Balmer line for 115 cluster galaxies (five of the members with ACS imaging do not have measured [OII]). The dotted lines denote the division between the three spectral types: emission-line, absorption-line, and post-starburst (E+A) galaxies. The symbols denote the three morphological classes assigned by P05: elliptical ($-5 \leq T \leq -3$), S0 ($-2 \leq T \leq 0$), and spiral+irregular ($T \geq 1$).

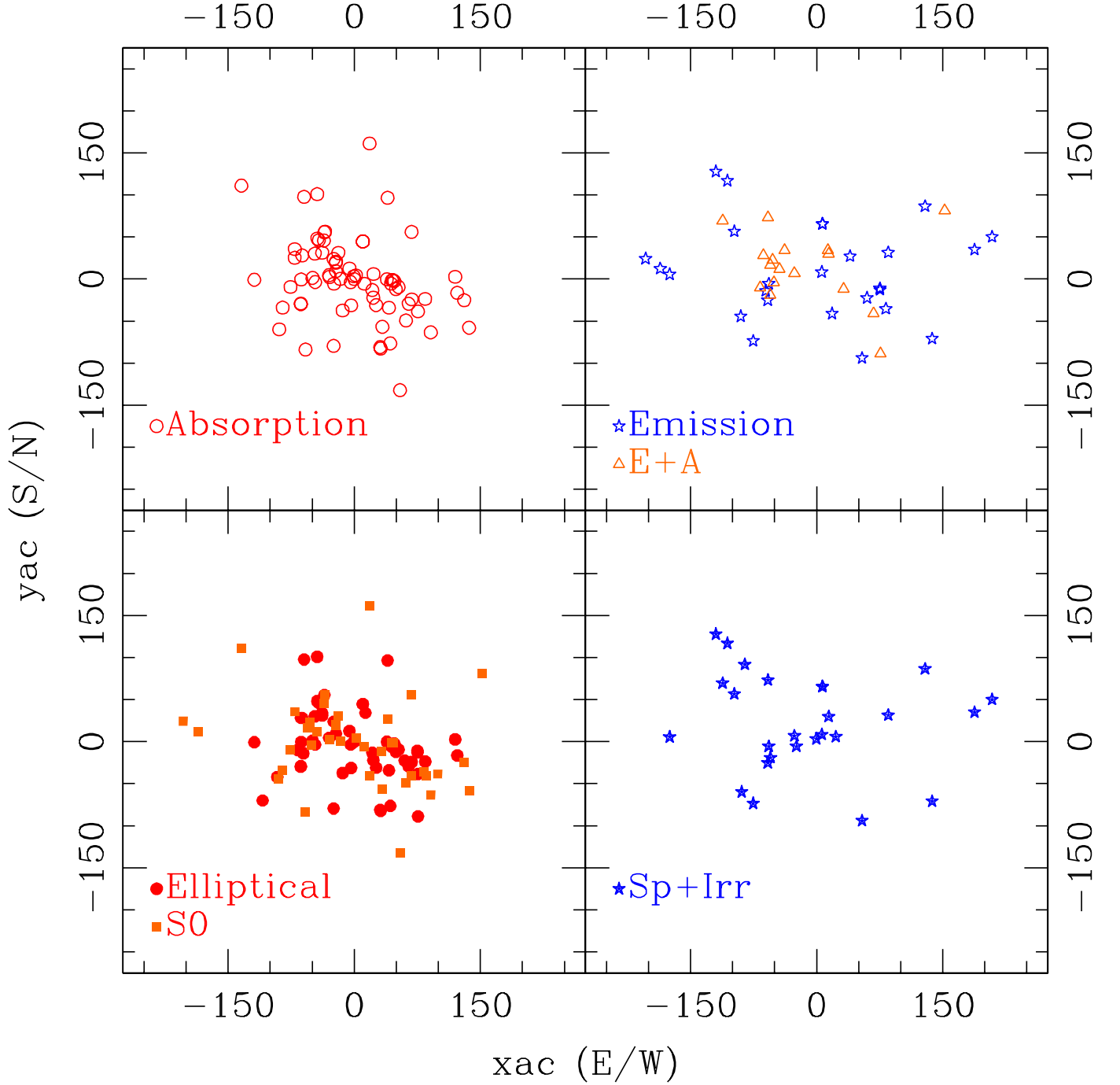


FIG. 5.— Spatial distribution of the 120 galaxies in MS1054 with ACS imaging. The coordinates are relative to the BCG (H4520) and are in arcseconds; the x -axis corresponds to right ascension (–east, +west) and the y -axis to declination (–south, +north). The cluster galaxies are separated by spectral (top panels) and morphological class (bottom panels).

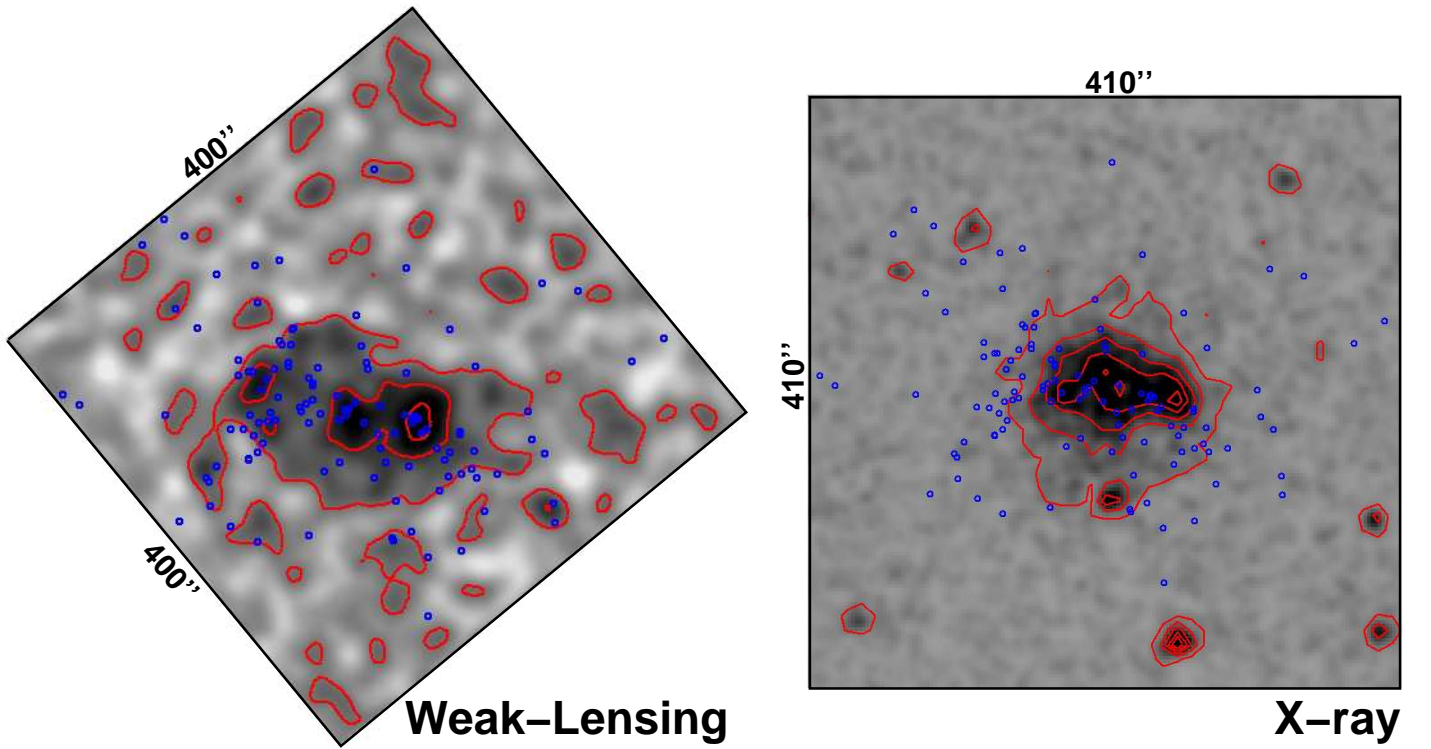


FIG. 6.— *Left:* The ACS weak-lensing map of MS1054 from Jee et al. (2005) is 400'' on a side where north is up and east to the left, as in Fig. 5. Mass contours corresponding to $\kappa = 0.1, 0.2$, & 0.3 are shown in red, and the positions of the 120 confirmed members that fall on the ACS imaging are shown as blue circles. *Right:* The smoothed XMM-Newton map of MS1054 from Gioia et al. (2004) is approximately 410'' on a side and has the same orientation. The X-ray contours correspond to flux observed in the $0.5 - 10$ keV band, and the same cluster galaxies are shown. For a color image of the MS1054 ACS mosaic, we refer the reader to Blakeslee et al. (2006).

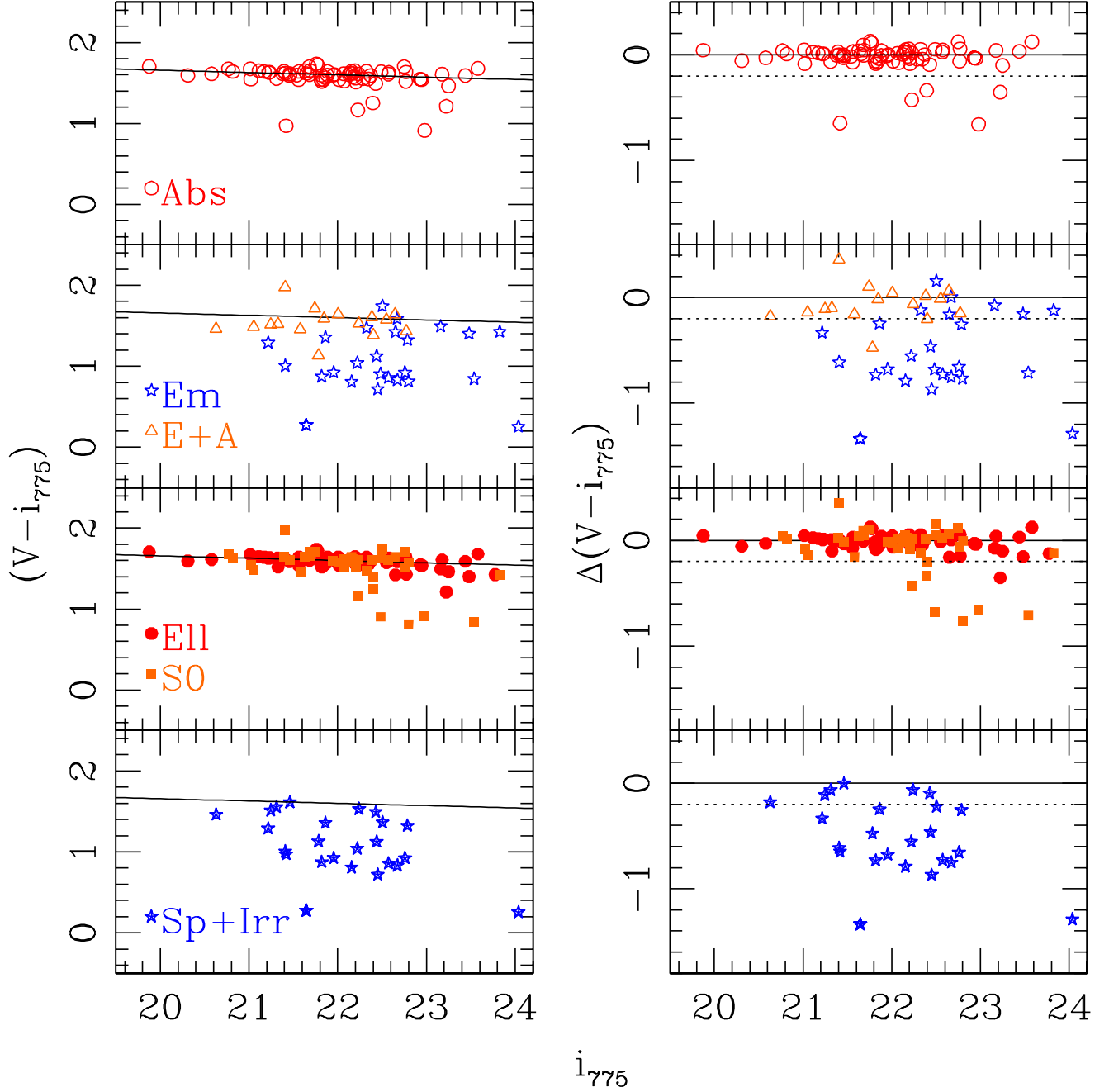


FIG. 7.— *Left panels:* Color-magnitude (CM) diagrams for the cluster galaxies that fall on the ACS mosaic ($i_{775}^* \sim 22.3$; Goto et al. 2005). In the top two panels, the members are separated into the three spectral types: absorption-line (open circles), emission-line (open stars), and post-starburst (E+A; open triangles) galaxies. In the bottom two panels, the members are separated into the three morphological types as classified by Postman et al. (2005): ellipticals (filled circles), S0s (filled squares), and spiral+irregulars (filled stars). The solid line in all four panels is the CM relation determined by fitting the 67 red absorption-line members. *Right panels:* For the same galaxy classes, the difference between their measured color and the color predicted from the CM relation; the dotted line denotes $\Delta(V - i_{775}) = -0.2$, our division between red and blue members. The absorption-line members define a strikingly narrow sequence along the fitted CM relation: 67/72 have $\Delta(V - i_{775}) > -0.1$.

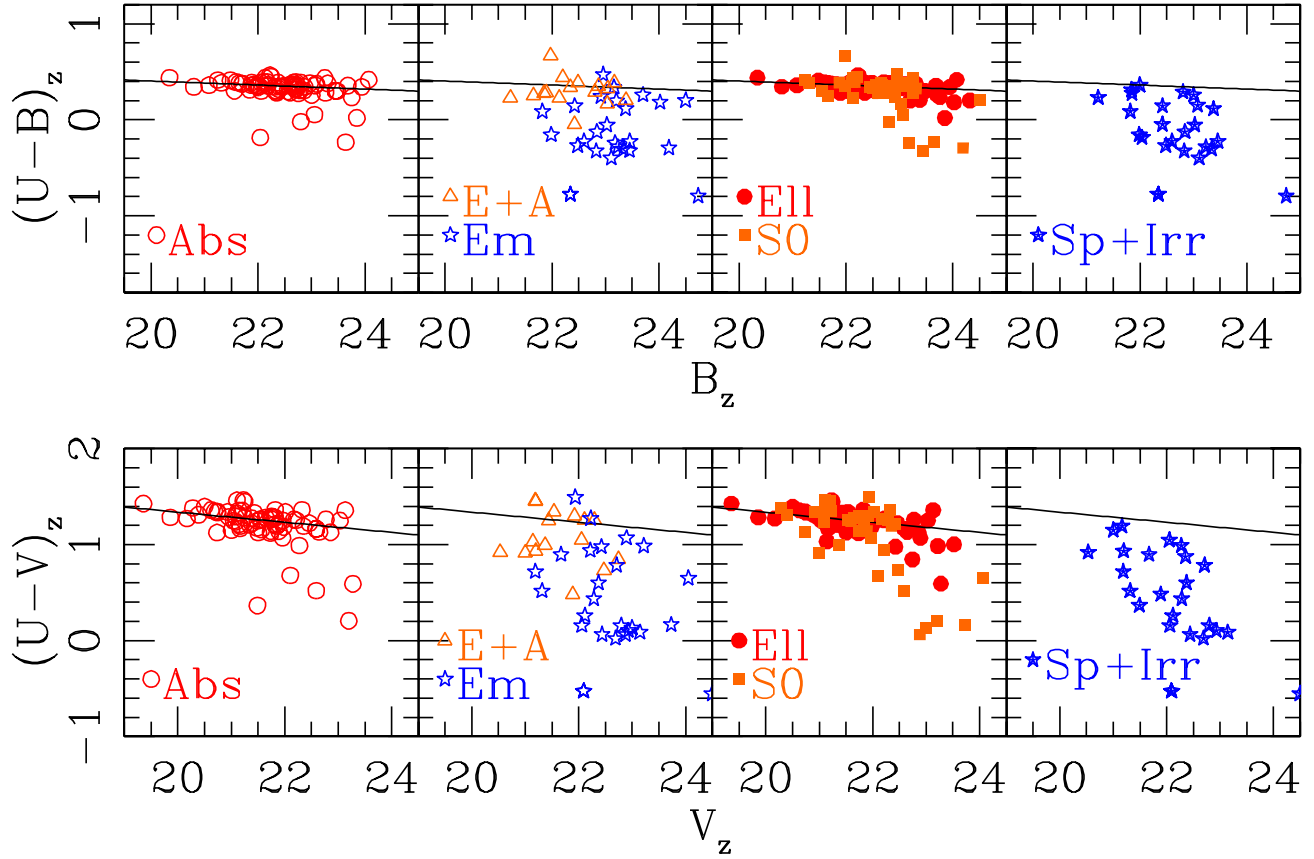


FIG. 8.— *Top panels:* CM diagrams for the same galaxy classes as in Fig. 7 but in rest-frame colors corresponding to $(U-B)_z$ (top panels) and $(U-V)_z$ (bottom panels). The spectral types (absorption, E+A, emission) are always open symbols while the morphological types (E, S0, Sp+Irr) are always solid symbols. Again, the absorption-line members have the lowest scatter in color of all the galaxy types.

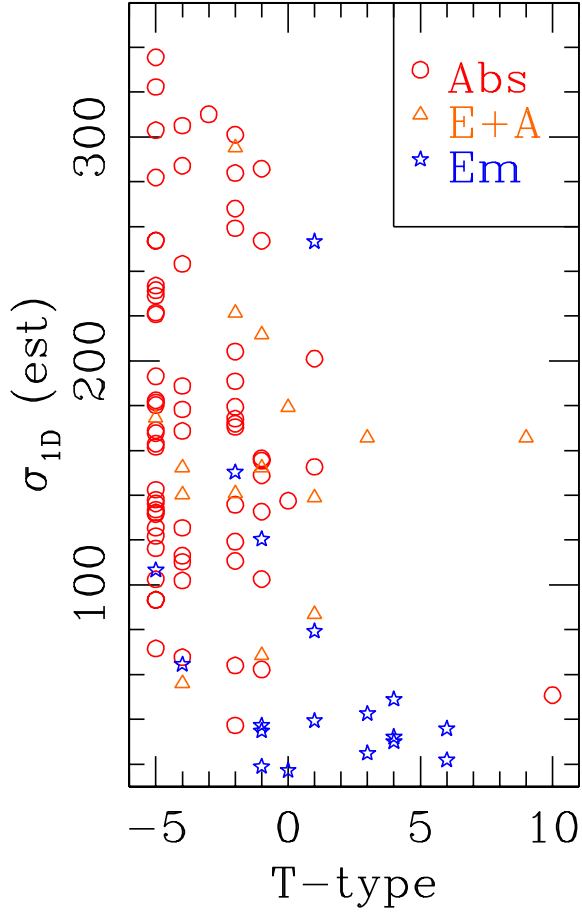


FIG. 9.— The morphological types assigned by P05 versus internal velocity dispersions: the E+S0 members have $T \leq 0$ while Spiral+Irregulars have $T \geq 1$. Internal velocity dispersions have been measured for 27 of the members (errors $< 50 \text{ km s}^{-1}$; Wuyts et al. 2004), and σ_{1D} estimated for the remainder (see Tran et al. 2003a). The symbols correspond to the spectral classifications. Most of the emission-line members are low mass ($\sigma_{1D} < 100 \text{ km s}^{-1}$) systems, and more than half are Sp+Irr. Assuming the emission-line members evolve onto the red sequence at $z < 0.8$, they can only be low-mass, low-luminosity members.

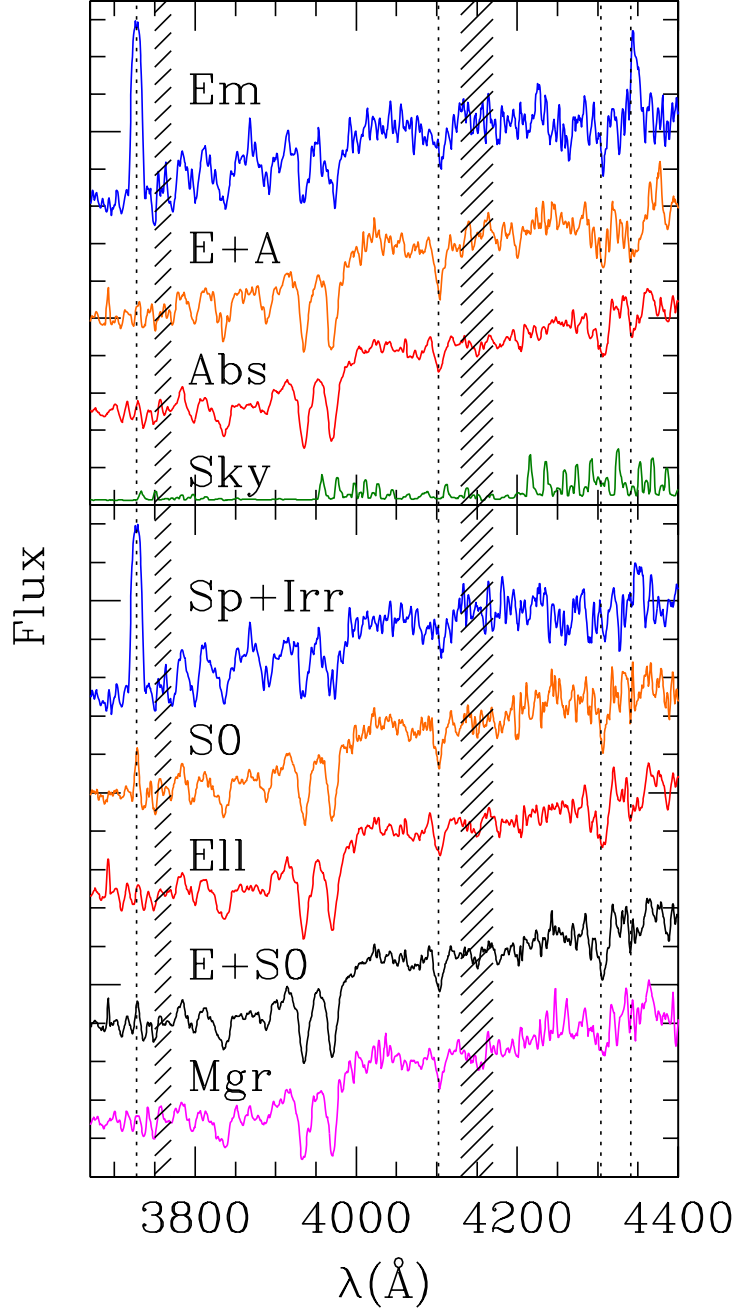


FIG. 10.— *Top*: Smoothed composite spectra for the three different spectral types plotted in the rest-frame on an arbitrary flux scale; the dotted vertical lines denote $[OII]\lambda 3727$, $H\delta$, G-band, and $H\gamma$. We include a spectrum of the night sky-lines and indicate the noisier regions corresponding to corrections for telluric absorption (hatched bars); the observed wavelengths of the sky features have been divided by 1.83. $H\delta$ absorption is evident in all three composite spectra but is weakest in the absorption-line spectrum (Table 4). *Bottom*: Smoothed composite spectra for the different morphological classes; we show a combined early-type spectrum (E+S0) as well as spectra for the individual types. We also include the composite spectrum for the 17 members that are in red, merging systems from Tran et al. (2005a). $H\delta$ absorption is evident in all of the composite spectra, even when only considering the ellipticals (Table 4).

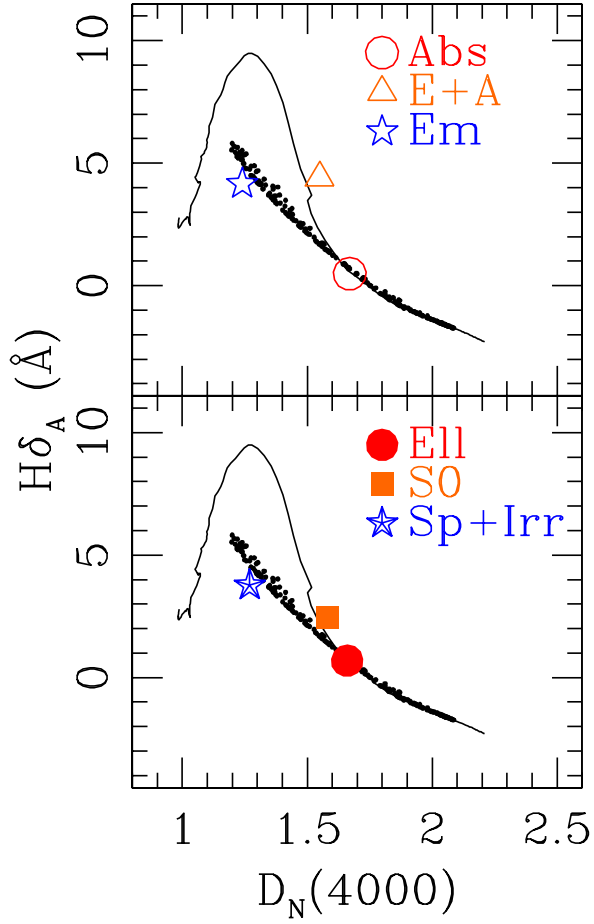


FIG. 11.— Using our composite spectra, we measure the spectral indices $H\delta_A$ and $D_N(4000)$ to compare mean stellar ages. The different spectral and morphological classes are shown in the top and middle panels respectively; errorbars are smaller than the symbol sizes (see Table 4). The red mergers lie at the same point as the absorption-line members. The solar metallicity BC03 models from Kauffmann et al. (2003) for continuous star formation (small dots) and single starburst (curve) are included in each panel. The spectral diagnostics show that the composite S0 spectrum has a younger mean stellar age than the composite elliptical.

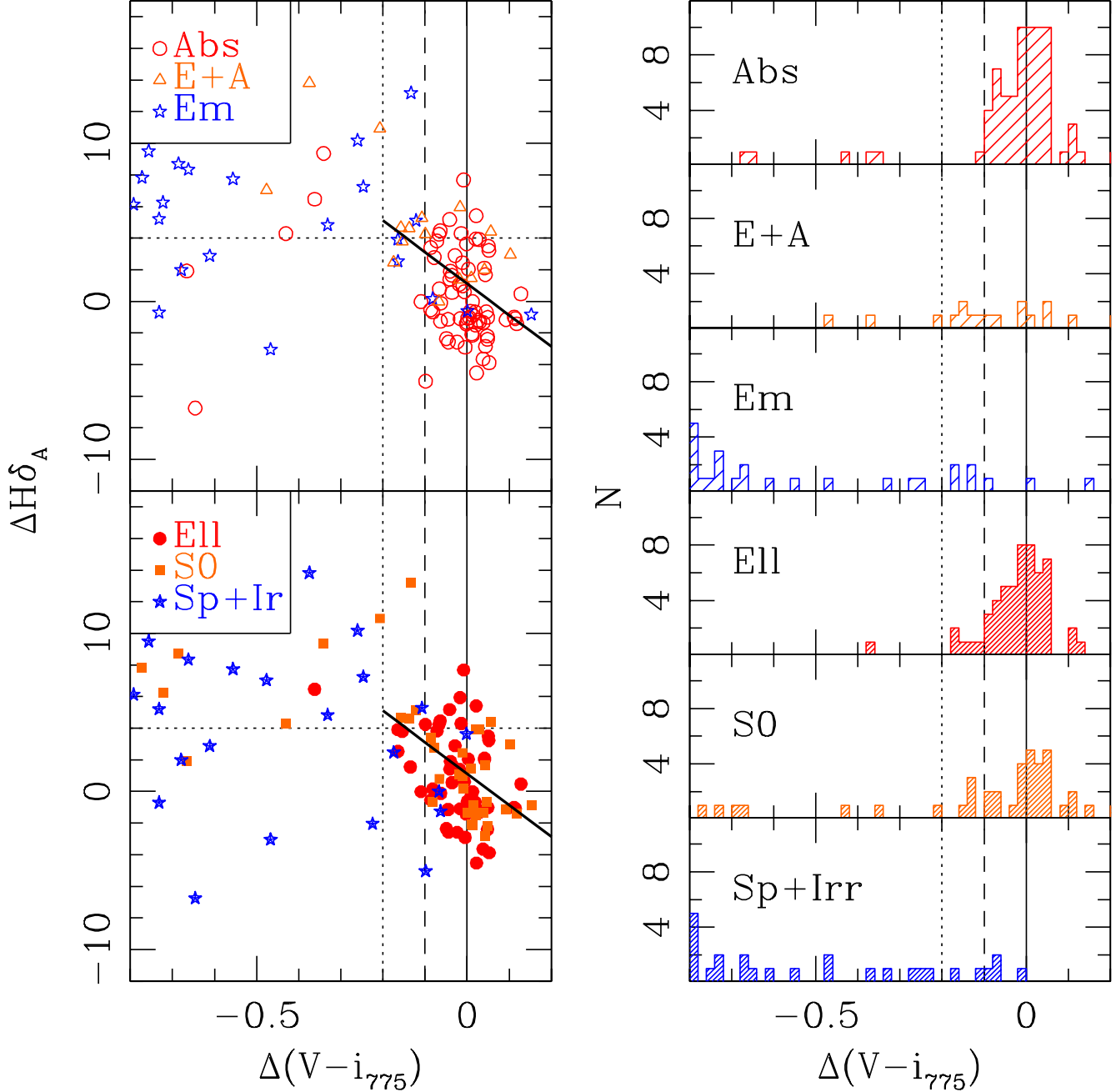


FIG. 12.— *Left Panels:* Normalized $H\delta_A$ equivalent width versus offset in $(V - i_{775})$; for clarity, we do not show the full range of values (see Table 1). The dotted horizontal line corresponds to $H\delta_A = 4\text{\AA}$, the vertical dotted line at $\Delta(V - i_{775}) = -0.2$ divides blue and red members, and the dashed line at $\Delta(V - i_{775}) = -0.1$ highlights the tight color distribution of the absorption-line members. Remarkably, 8/10 of the members in the adjacent color bin, $-0.2 \leq \Delta(V - i_{775}) < -0.1$, show post-starburst signatures. We find a trend of decreasing $H\delta$ absorption with color for the red members (heavy solid diagonal line; $> 95\%$ confidence). *Right Panels:* Histograms of $\Delta(V - i_{775})$ for the same galaxy classes shown in the left panels; the vertical lines correspond to the same $\Delta(V - i_{775})$ references.

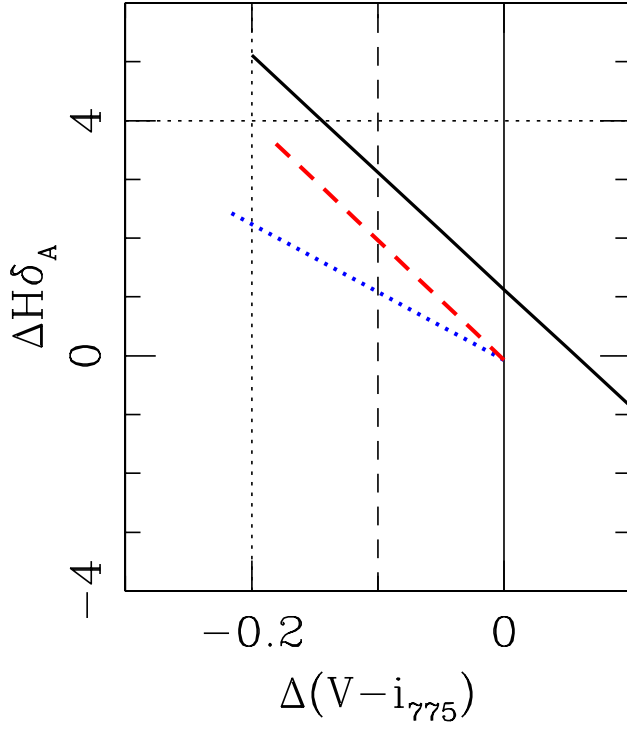


FIG. 13.— To determine whether the measured trend between $H\delta_A$ and $\Delta(V - i_{775})$ is due to age or metallicity, we compare to the BC03 single-burst models. The vertical and horizontal lines are as in Fig. 12 (left panels), and the heavy diagonal is the fit to the red members. In Case 1 (dotted diagonal), we assume galaxies with constant age (3 Gyr) and changing metallicity ($0.2Z_{\odot} - Z_{\odot}$), and in Case 2 (dashed diagonal), we assume constant solar metallicity and ages of 1.4 – 3 Gyr. The measured fit is best matched by the trend due to age variations alone (Case 2; dashed diagonal).